INORGANIC CHEMISTRY

FRONTIERS

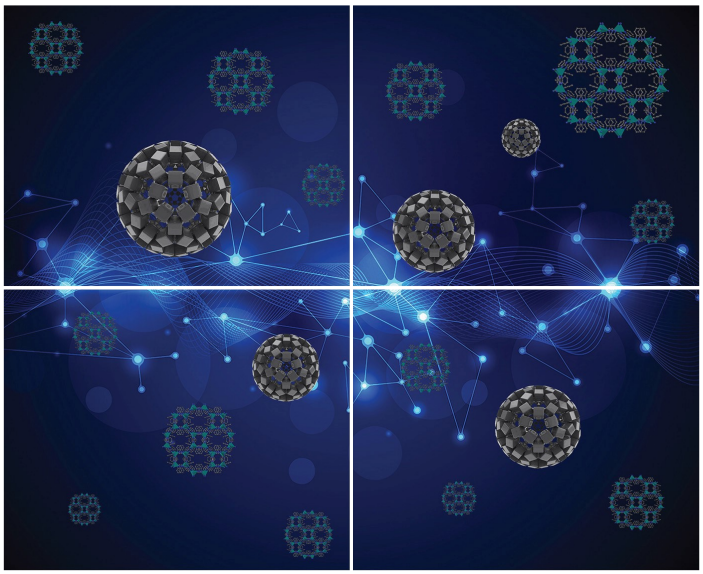

Accepted Manuscript

This article can be cited before page numbers have been issued, to do this please use: S. K. Langley, A. Swain, Y. Whyatt, D. Wielechowski, S. L. Benjamin, K. S. Murray, G. Rajaraman and S. Muthu, *Inorg. Chem. Front.*, 2024, DOI: 10.1039/D4QI01484G.

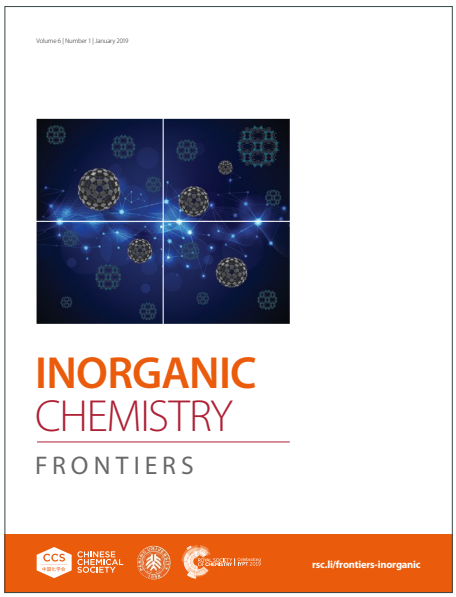

View Article Online
DOI: 10.1039/D4QI01484G

Enhancing Blocking Temperatures in $\{Cr^{III}_2Dy^{III}_2\}$ Butterfly SMMs: Deciphering the Role of Exchange Interactions and Developing Magneto-Structural Maps

Abinash Swain[a], Yasmin L. Whyatt[b], Daniel Wielechowski[c], Muthu Satheeshkumar[a], Sophie Benjamin[d], Keith S. Murray[c*], Gopalan Rajaraman[a*] and Stuart K. Langley[e*]

a) Department of Chemistry, IIT Bombay, Powai, Mumbai – 400076., India. Email: rajaraman@chem.iitb.ac.in
b) Department of Chemistry, The University of Manchester, Manchester, UK
c) School of Chemistry, Monash University, 17 Rainforest Walk, Clayton, Victoria 3800, Australia. E-mail: keith.murray@monash.edu
d) School of Science and Technology, Nottingham Trent University, Nottingham NG11 8NS, UK
e) Department of Natural Sciences, Manchester Metropolitan University, Manchester M1 5GD, England, United Kingdom Email; S.Langley@mmu.ac.uk

Abstract:

A tetranuclear heterometallic butterfly-shaped complex of the molecular formula; $[Cr^{III}_2Dy^{III}_2(OMe)_2(mdea)_2(benz)_4(NO_3)_2]$ ($mdeaH_2$ = *N*-methyldiethanolamine, benz = benzoate) was reported by us and found to display single-molecule magnetism (SMM) behaviour with a U_{eff} = 54 cm^{-1} and well-resolved magnetisation hysteresis plots, with a blocking temperature, T_B = 3.5 K. In the present study, fourteen related $\{Cr^{III}_2Dy^{III}_2\}$ complexes have been synthesised, and their magnetic properties have been studied. The study probes how chemical changes in bridging ligands and coordination environment affect the SMM properties compared to the parent complex. We show that by making simple chemical modifications to the ligands, the U_{eff} and T_B values change, with U_{eff} values ranging from 22 to 65 cm^{-1} and T_B 1.8 K – 4.7 K. We also show that SMM behaviour can be turned off by manipulation of the coordination sphere around the Dy^{III} ion. Based on these experimental results, we undertook a detailed theoretical study to understand why these changes occur. The theoretical studies further describe the mode of exchange mechanism in such complexes and how it controls the blocking temperature. Further, we have found that the exchange coupling between the Dy^{III}-Cr^{III} ions strongly influences the magnetic relaxation for this family of complexes, and interestingly, the exchange between the Cr^{III}–Cr^{III} centres plays a determining role in the overall SMM properties, which has been ignored in previous studies. We have derived a

View Article Online
DOI: 10.1039/D4QI01484G

relation between the magnetic exchange and T_B for such 3d–4f SMMs where exchange coupled states play a dominant role, revealing the blocking temperature is strongly correlated to the overall magnetic exchange. This clearly illustrates the importance of inducing strong exchange coupling to enhance not only the magnetisation reversal barrier but also T_B via quenching of zero-field quantum tunnelling of the magnetisation (QTM) in {3d–4f} type complexes.

Introduction:

Single-molecule magnets (SMMs)[1] offer the tantalising possibility of storing digital information on a single molecule and providing the ultimate high-density data storage platform.[2] For this technology to become a reality, the temperature at which data can be stored must be addressed.[3, 4] Since the discovery of the first SMM in 1993, a $\{Mn_{12}OAc\}$[5] complex, which displays a magnetic blocking temperature (T_B) of 4 K, huge improvements have been made, especially in the past few years, with the best-performing SMMs able to store digital information at temperatures > 80 K.[6] The driving force for these breakthroughs is due to a shift from synthesising complexes consisting of pure transition metal ions to harnessing the large anisotropy inherently present for lanthanide ions, with a major focus lying on the Dy^{III} ion. [7-10] The recent increases in T_B stem from the design of mononuclear lanthanide SMMs using a simple electrostatic approach.[11, 12] The approach for Dy^{III} ions is simply prescribed using highly charged ligands on a single axis (i.e. a linear type geometry) while minimising ligands equatorial to these ligands. This approach lays a blueprint for designing SMMs with extremely large anisotropy barriers (U_{eff}), hence allowing the electrons to retain their orientation at much higher temperatures than previously observed. For example, Goodwin et al.[13] achieved remarkable increases in T_B by fully conforming to this design in the isolation of the first dysprosocenium cation $[Dy(C_5H_2{}^tBu_3)_2]^+$, which is a sandwich complex with no equatorial ligands. They reported a U_{eff} = 1223 cm^{-1}, with T_B = 60 K.[13] Several other dysprosocenium derivatives have subsequently been reported with a range of T_B reported between 62 K to 80 K.[6, 13-15] While the use of lanthanide ions has pushed the field forward significantly, with molecules producing very large U_{eff} parameters, many problems have been highlighted in terms of the relaxation mechanism, especially the observations of fast quantum tunnelling of the magnetisation (QTM)[16] which results in a loss of magnetisation via an under barrier process.[6, 14] With this in mind, while the best SMM limits the probability of QTM occurring, we need to understand how QTM can be controlled and minimised. One successful approach has been to use

View Article Online
DOI: 10.1039/D4QI01484G

polynuclear lanthanide complexes, which introduce relatively strong magnetic exchange interactions between ions. This was most notably highlighted in N_2^{3-} radical bridged Ln^{III} dinuclear complexes.[17, 18] In general, exchange interactions (J) between Ln^{III} ions are often < 0.1 cm^{-1} due to the contracted nature of the magnetic orbitals.[19, 20] In the case of the radical bridged system, it is reported that the magnetic exchange interaction of $J_{Gd\text{-}rad}$ = –27 cm^{-1} between the radical and Gd^{III} ion and hysteresis was observed at T_B = 14 K with a U_{eff} = 227 cm^{-1} for the Tb^{III} analogue with little indication of QTM relaxation.[21] While the radical-4f interactions are very strong in some cases, they are weaker in others, and this is correlated to the nature of the orbital that holds the unpaired electron at the radical centre with a strongly delocalised radical, leading to weaker exchange. However, the stability of the radical complexes is generally proportional to the delocalisation of spin density, with strong delocalisation leading to greater stability and, thus, weaker exchange coupling.[22-24] Other alternative strategies that can be implemented to enhance the magnetic exchange is the introduction of direct metal-metal bonding, though these are very rare systems as they are very unstable.[25, 26] For comparatively stable molecules, there is scope for 4f metal ions coupled with 4d/5d ions, as the later have more diffuse orbitals.[27] Furthermore 4f-radical exchange as high as +300 cm^{-1} has been observed in the lanthano fullerene class of molecules, paving the way forward for desired strong magnetic exchange interactions. [28-30]

Alternative avenues that have been explored include {3d–4f} assemblies where a suitable 3d metal ion is incorporated in the 4f cluster aggregation, with the aim being to induce relatively stronger exchange coupling than is possible for {4f–4f} exchange.[31-35] Among several {3d–4f} complexes reported, incorporating the Cr^{III} ion seems more beneficial. Results suggest this boosts the exchange more strongly than any other transition metal ion while suppressing the QTM significantly.[36,37] This was highlighted by some of us[38-44] in a hetero-metallic tetra-nuclear complex of formula $[Cr^{III}_2Dy^{III}_2(OMe)_2(mdea)_2(benz)_4(NO_3)_2]$ (Figure **1**). This is a rare example of a lanthanide SMM that displays relatively strong magnetic exchange interactions and magnetic hysteresis with large coercive fields that were unprecedented in this class of compounds.

While stronger exchange coupling underscores better SMMs in this $\{Cr^{III}_2Dy^{III}_2\}$ class of compounds, a correlation between various structural alterations and the observed magnetic properties (such as exchange coupling, magnetisation reversal barrier and blocking temperature T_B) is not established, and such an understanding is imperative to improve the performance of the

View Article Online
DOI: 10.1039/D4QI01484G

SMMs both in this class of compounds but also in the other class of $\{M_2Dy_2\}$ butterflies that perhaps make one of the largest family of complexes (~500 structures in CCDC database) for SMMs among all poly-nuclear{3d–4f} complexes reported. Furthermore, in this class of complex, the geometry around the Ln^{III} ions are generally preserved as square antiprismatic (pseudo-D_{4d}), which is shown to yield large single-ion magnetic anisotropy, especially for the oblate type ions such as Dy^{III}/Tb^{III}/Ho^{III} etc.[45,46] A quick glance at the Cambridge structural database reveals ~500 such geometries where square antiprismatic geometries are preserved. As preserving geometries in polynuclear {3d–4f} classes is challenging, the butterfly $\{M_2Ln_2\}$ core remains, perhaps, the most successful structural motif among {3d–4f} classes that yield attractive SMM characteristics.[40] Despite the vast amount of experimental data that are available, even a simple correlation of geometry/electronic structure to the experimental observables such as J, U_{eff} and T_B is lacking. Particularly, there are several puzzling observations of very large U_{eff} values with no blocking temperature[47] and moderate U_{eff} values with relatively large T_B values, [38-44,48] hinting at an absence of direct correlations between these two important SMM parameters. To answer such an intriguing observation in this area, we have synthesised, structurally, and magnetically characterised fifteen different $\{Cr^{III}_2Dy^{III}_2\}$ complexes and used extensive theoretical studies (DFT and CASSCF/RASSI-SO/POLY_ANISO approach)[49-52] thereby establishing several structural correlations to the observed magnetic properties.

We subdivide the fifteen reported complexes into four sections/groups where either the amine polyalcohol R group (category 1 and 2, structures **1**-**2d**), bridging ligands (category 3, structures **3a**-**3g**) or the coordination environment around the Dy^{III} (category 4, structures **4a**-**4c**) are altered as shown schematically in Scheme **1** along with the ligands employed (Figure **1**).

The fifteen complexes studied have the following formulae; $[Cr^{III}_2Dy^{III}_2(OMe)_2(mdea)_2(benz)_4(NO_3)_2]$ (**1**),[39] $[Cr^{III}_2Dy^{III}_2(OMe)_2(dea)_2(benz)_4(MeOH)_4](NO_3)_2$ (**2a**) $[Cr^{III}_2Dy^{III}_2(OMe)_2(edea)_2(benz)_4(NO_3)_2]$ (**2b**), $[Cr^{III}_2Dy^{III}_2(OMe)_2(bdea)_2(benz)_4(NO_3)_2]$ (**2c**), $[Cr^{III}_2Dy^{III}_2(OMe)_2(teaH)_2(benz)_4(NO_3)_2(MeOH)_2]$ (**2d**), $[Cr^{III}_2Dy^{III}_2(OMe)_2(mdea)_2(2\text{-Cl-benz})_4(NO_3)_2]$ (**3a**), $[Cr^{III}_2Dy^{III}_2(OMe)_2(bdea)_2(2,6\text{-Cl-benz})_4(NO_3)_2]$ (**3b**), $[Cr^{III}_2Dy^{III}_2(OMe)_2(mdea)_2(2,4,6\text{-Cl-benz})_4(NO_3)_2]$ (**3c**), $[Cr^{III}_2Dy^{III}_2(OMe)_2(mdea)_2(2\text{-Cl-4,5-F-benz})_4(NO_3)_2]$ (**3d**), $[Cr^{III}_2Dy^{III}_2(OMe)_2(mdea)_2(2\text{-}CF_3\text{-benz})_4(NO_3)_2]$ (**3e**), $[Cr^{III}_2Dy^{III}_2(OMe)_2(mdea)_2(2\text{-OMe-benz})_4(NO_3)_2]$ (**3f**), $[Cr^{III}_2Dy^{III}_2(OMe)_2(^tBudea)_2(4\text{-}^tBu\text{-}$

View Article Online
DOI: 10.1039/D4QI01484G

*Scheme **1**. Synthesis route for all the butterfly complexes.*

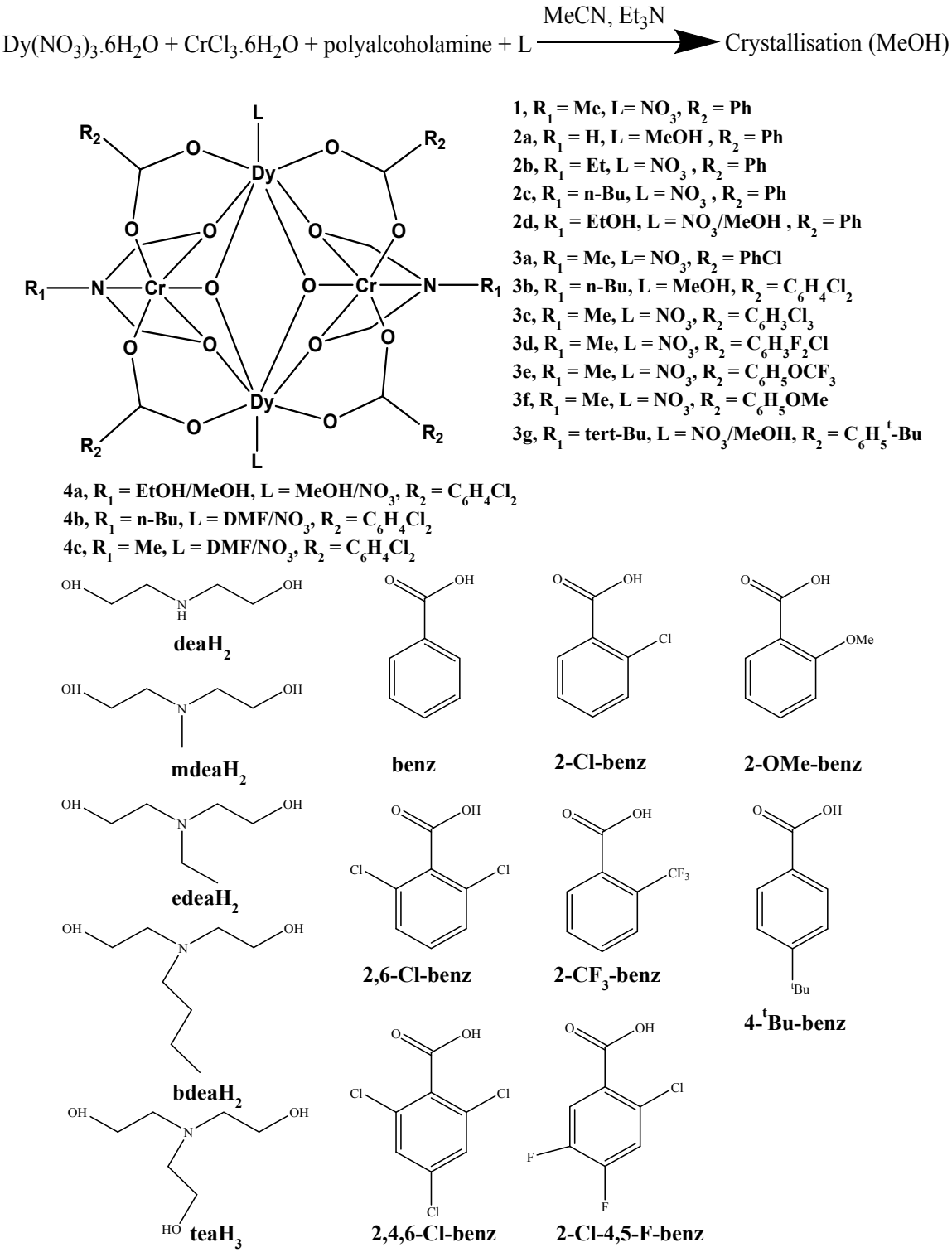

Figure **1**. Structural representation of the $\{Cr^{III}_2Dy^{III}_2\}$ butterfly complexes and structural formulae of the ligands. bdeaH2

View Article Online
DOI: 10.1039/D4QI01484G

benz)$_4$(NO$_3$)$_2$] (**3g**), [Cr$_2$Dy$_2$(OH)$_2$(2,6-Cl-benz)$_4$(teaH)$_2$(MeOH)$_2$(NO$_3$)$_2$](HNEt$_3$)Cl (**4a**), [Cr$_2$Dy$_2$(OH)$_2$(2,6-Cl-benz)$_4$(bdea)$_2$(DMF)$_2$(NO$_3$)$_2$)] (**4b**), [Cr$_2$Dy$_2$(OH)$_2$(2,6-Cl-benz)$_4$(mdea)$_2$(DMF)$_2$(NO$_3$)$_2$] (**4c**). [mdeaH$_2$ = N-methyldiethanolamine, deaH$_2$ = diethanolamine, edaH$_2$ = ethyldiethanolamine, bdeaH$_2$ = N-n-butyldiethanolamine, teaH$_3$ = triethanolamine, ^{t}Budea = N-^{t}butyldiethanolamine, benz = benzoic acid and DMF = dimetylformamide]. The ligand formulae, along with the structures, are provided below in Figure **1**. Using these groups of complexes, we explain the following: i) which features influence the SMM behaviour of these complexes; ii) the reason why QTM is minimised; iii) optimisation of the SMM properties; iv) how the nature and magnitude of the magnetic exchange interaction control the T_B.

Experimental

General Information

All reactions were carried out under aerobic conditions. Chemicals and solvents were obtained from commercial sources and used without further purification. Elemental analyses (CHN) were carried out by Campbell Microanalytical Laboratory, University of Otago, Dunedin, New Zealand. The synthesis of all 14 complexes and representative infra-red spectra and PXRD analysis are shown for compounds **1** and **2a** in the ESI.

Crystal data collection and refinement.

X-ray crystallographic measurements for compounds **1**, **2c, 2d, 3a**, **3e** and **3f** were collected with an Oxford Diffraction Supernova diffractometer using MoKα radiation. The data collection and data reduction were performed using CrysAlisPro; absorption corrections were applied using a multi-scan method.[53] The data for **2a** and **2b** were performed using a Bruker Smart Apex X8 diffractometer with MoKα radiation. The data collection and integration were performed within SMART and SAINT+ software programs and corrected for absorption using the Bruker SADABS program.[54] Measurements on complexes **3b**, **3c**, **4a**, **4b** and **4c** were made using an Oxford Xcalibur diffractometer with MoKα radiation (λ = 0.71073 Å) and a Sapphire3 detector. The data collection and integration were performed within the CrysAlisPro software program. X-ray measurements for **3d** and **3g** were performed at 150(2) K at the Australian synchrotron MX1 beam-line. The data collection and integration were performed within Blu-Ice and XDS software programs.[55,56] All complexes were all solved by direct methods (SHELXS-97), and refined (SHELXL-97) by full

View Article Online
DOI: 10.1039/D4QI01484G

least matrix least-squares on all F^2 data.[57] Crystallographic data and refinement parameters for all these complexes are summarised in Table **S1a-1c**. Crystallographic details are available in the Supporting Information (SI) in CIF format. CCDC numbers 866839, 994294–994297, 1495741–1495743 and 2268871-2268878. These data can be obtained free of charge from the Cambridge Crystallographic Data Centre via www.ccdc.cam.ac.uk/data_request/cif. See Table **S1a-1c** for experimental details.

Magnetic measurements

Direct current (dc) magnetic susceptibility measurements were carried out on a Quantum Design SQUID magnetometer MPMS-XL 7 operating between 1.8 and 300 K for dc-applied fields ranging from 0 – 5 T. Microcrystalline samples were dispersed in Vaseline in order to avoid torquing of the crystallites. The sample mulls were contained in a calibrated gelatine capsule held at the centre of a drinking straw that was fixed at the end of the sample rod. Alternating current (ac) susceptibility measurements were carried out on the same instrument utilising an oscillating ac field of 3.5 Oe and frequencies ranging from 0.1 to 1500 Hz. Hysteresis measurements were performed with an average sweep rate of 0.003 T s^{-1}.

Computational details:

The magnetic properties of this series of complexes were analysed through an *ab initio* study using the MOLCAS 8.0/8.2 suite of programs.[58] The approach was of CASSCF/RASSI-SO/SINGLE_ANISO type calculations to determine the low-lying energy levels and magnetic properties of individual Dy^{III} and Cr^{III} ions.[51, 52, 59-61] The estimated values of the exchange coupling between the Dy…Cr and Dy…Dy ions were performed in the Gaussian 16.0 C[62] suite of programs by considering the BS-DFT[63] approach using the hybrid type hybrid B3LYP functional.[64, 65] Since first-order orbital momentum plays a distinctive role for Dy^{III} it cannot be described in the single determinant, hence the BS-DFT involves the replacement of Dy^{III} with Gd^{III}, and the exchange value was then normalised with respect to the Dy^{III} ion.[66-67] The *ab initio* SINGLE_ANISO module also generates inputs to proceed for the POLY_ANISO module, which has been used to calculate the exchange parameter. [69, 70]

Equation for J , $H = -JS_1S_2$ Eqn (1)

View Article Online
DOI: 10.1039/D4QI01484G

The calculations were performed on the obtained X-ray diffraction crystal structures without further optimisation. In calculating the single ion properties, other Dy^{III} and Cr^{III} ions were replaced by Lu^{III} and Sc^{III}, respectively, for the SINGLE_ANISO module. The Cholesky decomposition threshold was set to 5.0 x 10^{-8}.[71] The relativistic effects were taken into consideration by including the Doughlas-Kroll-Hess Hamiltonian.[72] The active space for Dy^{III} includes nine electrons in seven orbitals, and for Cr^{III}, three electrons in five orbitals. For the RASSI-SO mixing, only 21 sextets were considered for Dy^{III} since it has been well-established for Dy systems and for Cr, 10 quartets and 40 doublets have been taken into account.[73] The SINGLE_ANISO module is used for the computation of local magnetic properties like the g-tensors and the magnetic axes of Dy^{III} and Cr^{III} centers. The basis set employed for the MOLCAS calculations is of ANO…RCC type, Dy. ANO-RCC...8s7p5d3f2g1h., Lu. ANO-RCC...7s6p4d2f., Sc. ANO-RCC...5s4p2d., O. ANO-RCC...3s2p., Cl. ANO-RCC...4s3p., F. ANO-RCC...4s3p., N. ANO-RCC...3s2p., C. ANO-RCC...3s2p., H. ANO-RCC...2s.[74-76] The basis set for BS-DFT calculations is of CSDZ[77] level basis set for Gd^{III} with the addition of electron core potential for the metal centers taken from the EMSL[78] library, and for the rest of the atoms, it was of TZV[79] type. To compare the DFT obtained J_{exch} from the Gaussian calculations with the earlier reported DFT J_{exch} by Chibotaru *et al.* using the ORCA[80] package, all the calculations have been repeated using the ORCA package with a similar model as that reported in 2013 on all the above complexes along with the parent complex using the same methodologies reported earlier.[28]

View Article Online
DOI: 10.1039/D4QI01484G

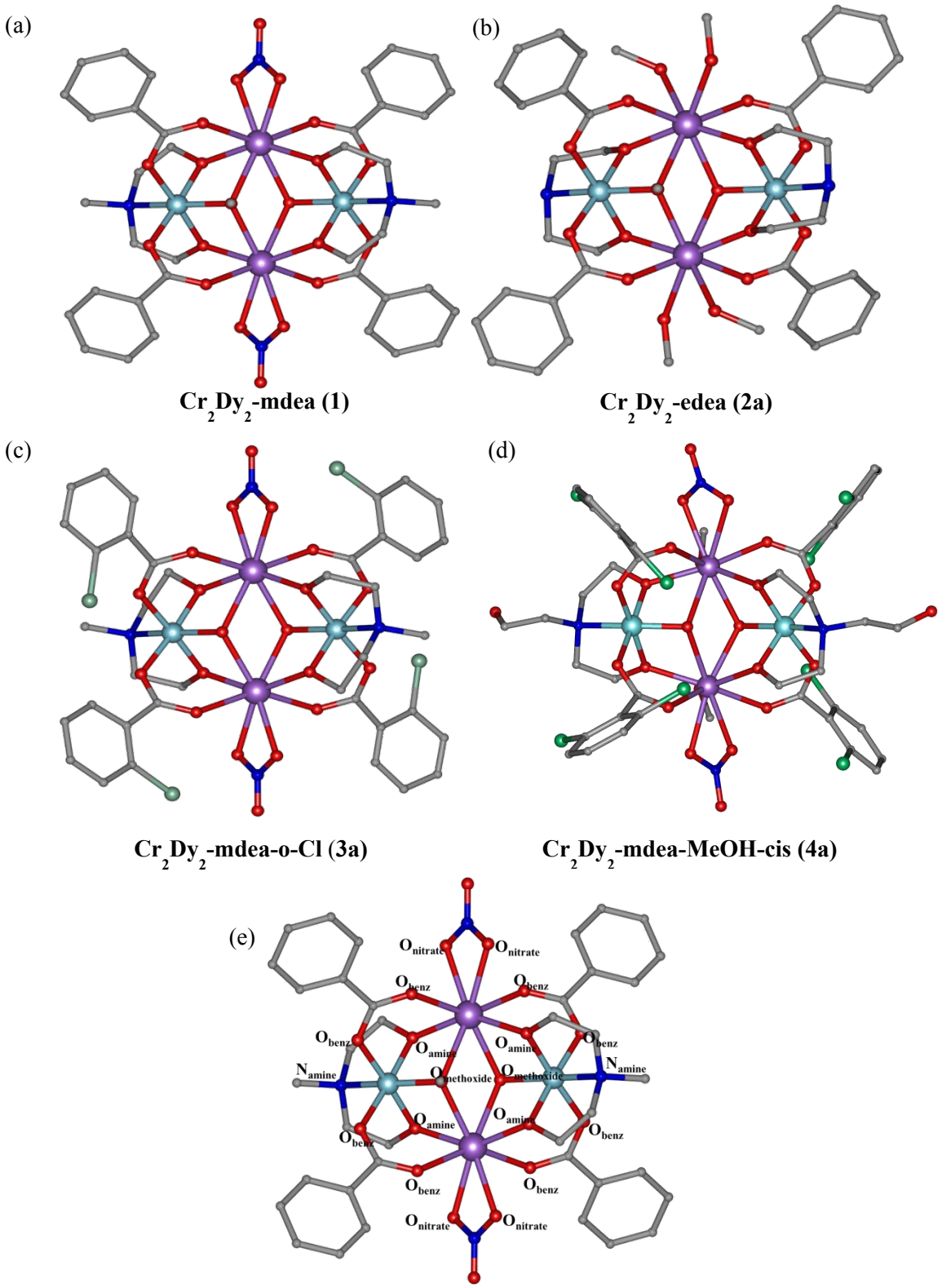

Figure **2**. Molecular structures of complex **1**(a)[39], **2a**(b), **3a**(c) and **4a**(d), Violet=Dy, Cyan=Cr, Grey=C, Red=O, Blue=N, Green=Cl, hydrogen atoms were omitted for clarity, (e) Schematic representation of the coordination environment.

View Article Online
DOI: 10.1039/D4QI01484G

Results and Discussion

Structural Description and Classification of the Complexes:

All of the fourteen newly characterised complexes have a $\{Cr^{III}_2Dy^{III}_2\}$ butterfly motif similar to **1** (Figure **2(a)**).[39] Complex **1** is described as a tetranuclear butterfly complex with the Dy^{III} ions in the body positions and the Cr^{III} ions lying in the outer wing positions. The Dy^{III} and Cr^{III} ions in the butterfly core are bridged by methoxide, benzoate and deprotonated amine polyalcohol ligands, whereas the Dy^{III} ions are bridged only by methoxide ligands. The coordination sphere of each Dy^{III} ion is completed by a chelating nitrate. The Cr^{III} ions are six coordinated with an octahedral geometry, and the Dy^{III} ions are eight coordinated with a square antiprismatic (SAP) geometry. With respect to the starting structure, we have classified these molecules into three types in order to have better comparison and insights according to the coordination around the Dy^{III} ion and the types of ligands involved in the complex. These three types are classified as follows: (i) **2a-2d**, (ii) **3a-3g** and (iii) **4a-4c** (Figure S1). See Figure **2** for the representative examples **1**, **2a**, **3a** and **4a**.

Structural Descriptions of 2a-2d: Complexes **2a-2d** are iso-structural with the parent complex **1,** and all crystalise in the monoclinic $P2_1/n$ space group. The asymmetric unit for each consists of half of the complex (one Cr^{III} and one Dy^{III} ion), which lies upon an inversion center. Each complex differs in the aminopolyalcohol used (**2a** = $deaH_2$, **2b** = $edeaH_2$, **2c** = $bdeaH_2$ and **2d** = $teaH_3$); however, the coordination to the metal ions remains the same in all cases, except we find that the coordination environment at the Dy^{III} ion differs for **2a** and **2d** compared to **1**. In the case of **2a,** two MeOH molecules are coordinated at each Dy^{III} site, whereas for **2d**, one terminal nitrate and a MeOH are coordinated (figure **S1**) instead of a chelating nitrate for **1**. The geometry around the Dy^{III} (SAP) and Cr^{III} (octahedral) (Table **1**) centers are the same with respect to **1**.

Structural Descriptions of 3a-3g: Complexes **3a-3g** are isostructural and crystallise in the triclinic *P-1* space group, with the key difference compared to **1** is that the bridging benzoate ligands have been replaced by several different functionalised benzoates. These include Cl-based (**3a-3c**), Cl and F-based (**3d**) and CF_3, OMe and ^{t}Bu (**3e, 3f** and **3g**, respectively) groups around the ring (Figures **1** and **S1**). The rationale for using these ligands was to test what effects electron withdrawing or donating groups and the steric effects that these ligands provide have on the magnetic behaviour and SMM properties of the complexes. For complexes **2a-2d** and **3a-3g,** the

View Article Online
DOI: 10.1039/D4QI01484G

deviation from an ideal SAP geometry for Dy^{III} and an ideal octahedral geometry for Cr^{III} has been provided in Table **1**, obtained from continuous SHAPE analysis.[74]

Structural Descriptions of 4a-4c: For complexes **4a-4c**, the bridging coordination environment is identical to **1**, but the coordination environment at the Dy^{III} ions was varied. Complexes **4a-4c** now reveal a nine-coordinate environment with a chelating nitrate and the inclusion of an extra solvent molecule (**4a** (MeOH), **4b** (DMF) and **4c** (DMF)) at each Dy^{III} site. In **4a,** methanol ligands lie *cis* to each other at each Dy^{III} site (Figure **2d**). Similarly, in **4b,** a DMF ligand coordinates via the O-atom to the Dy^{III} ions, which lie *cis* to each other. For **4c**, again, DMF coordinates to the Dy^{III} ions; however, the ligands are disposed of *trans* to each other (Figure **S1**). The nine-coordinate Dy^{III} ions display a tricapped trigonal prismatic (TCTPR) geometry (Table **1**), while the six-coordinate Cr^{III} ions are octahedral (see Table **1** for SHAPE analysis).[81]

Table **1**. Selected bond parameters (length in Å and angles in °) around the Dy^{III} ions for all the complexes. The terminology for the coordination environment has been provided in the ESI Figure **S2a-d**.

Parameters	**1**	**2a**	**2b**	**2c**	**2d**	**3a**	**3b**	**3c**	**3d**	**3e**	**3f**	**3g**	**4a**	**4b**	**4c**
Dy1-O1-Cr1	95.8	96.21	97.37	95.77	96.05	95.25	95.7	94.91	95	95.82	95.88	97.22	97.43	100.8	100.61
Dy1-O1'-Cr1'	95.7	95.87	97.39	95.79	96.05	96.2	96.57	96.61	95.87	96.76	95.91	97.32	99.87	100.86	100.68
Dy1-O5-Cr1	102.75	103.06	102.97	102.72	104.3	102.81	103.2	103.45	102.77	102.47	102.61	103.74	102.73	104.42	105.85
Dy1-O4'-Cr1'	103.3	104.6	102.24	103.71	104.53	102.52	103.87	104.16	102.34	102.5	102.3	104.05	105.95	107.73	107.03
Dy1-O1-Dy1'	114.1	114.267	113.09	113.58	114.74	114.03	113.25	113.01	113.86	113.52	113.8	113.58	113.54	109.26	109.31
Dy1-Dy1	4.105	4.148	4.034	4.086	4.171	4.091	4.083	4.07	4.091	4.063	4.074	4.091	4.078	3.981	3.974
Dy1-Cr1	3.282	3.299	3.301	3.286	3.286	3.278	3.302	3.286	3.273	3.276	3.272	3.278	3.323	3.403	3.403
Dy1-Cr1'	3.282	3.331	3.305	3.298	3.298	3.288	3.307	3.295	3.283	3.285	3.285	3.288	3.359	3.373	3.399
Cr1-Cr1'	5.157	5.174	5.233	5.164	5.173	5.139	5.197	5.173	5.122	5.152	5.139	5.139	5.201	5.119	5.059
Dy1-O2	2.355	2.33	2.355	2.347	2.345	2.243	2.243	2.227	2.24	2.243	2.255	2.248	2.385	2.322	2.321
Dy1-O5	2.248	2.267	2.282	2.238	2.262	2.349	2.351	2.414	2.384	2.359	2.34	2.365	2.297	2.433	2.455
Dy1-O4'	2.245	2.258	2.267	2.247	2.254	2.247	2.241	2.234	2.242	2.374	2.234	2.243	2.28	2.283	2.297
Dy1-O6'	2.347	2.354	2.365	2.383	2.362	2.35	2.409	2.377	2.386	2.351	2.351	2.356	2.449	2.488	2.474
Dy1-O1	2.452	2.444	2.414	2.449	2.47	2.448	2.461	2.462	2.443	2.436	2.44	2.426	2.422	2.448	2.448
Dy1-O1'	2.44	2.494	2.42	2.44	2.481	2.429	2.428	2.419	2.432	2.422	2.424	2.423	2.436	2.422	2.45
Dy1-O8	2.429	2.444	2.454	2.406	2.388	2.442	2.429	2.42	2.441	2.437	2.455	2.445	2.558	2.451	2.443
Dy1-O9	2.428	2.4	2.46	2.467	2.418	2.424	2.407	2.421	2.44	2.429	2.435	2.437	2.451	2.504	2.507
Dy1-O10	--	--	--	--	--	--	--	--	--	--	--	--	2.427	2.353	2.374
Average	2.368	2.374	2.377	2.3721	2.372	2.366	2.371	2.372	2.376	2.3813	2.367	2.3679	2.412	2.411	2.419
Avg. Ax.	2.299	2.302	2.317	2.304	2.306	2.297	2.311	2.313	2.313	2.332	2.295	2.303	--	--	--
Avg. Eq.	2.43725	2.4455	2.437	2.4405	2.43925	2.43575	2.43125	2.4305	2.439	2.431	2.4385	2.43275	--	--	--
ESD	0.084	0.086	0.073	0.089	0.085	0.084	0.085	0.090	0.087	0.066	0.086	0.082	0.079	0.071	0.067
	Deviation from idea SAP (Dy-eight coordinated), TCTPR (Dy-nine coordinated) and O_h (Cr- six coordinated) From SHAPE analysis														
Dy	1.801	0.721	2.023	2.000	0.846	2.001	1.761	1.883	1.782	1.806	1.968	2.179	1.801 (1.073)	0.721 (0.590)	0.263
Cr	0.37	0.349	0.449	0.390	0.394	0.408	0.465	0.514	0.396	0.396	0.390	0.706	0.37 (0.863)	0.349 (0.744)	0.920

View Article Online
DOI: 10.1039/D4QI01484G

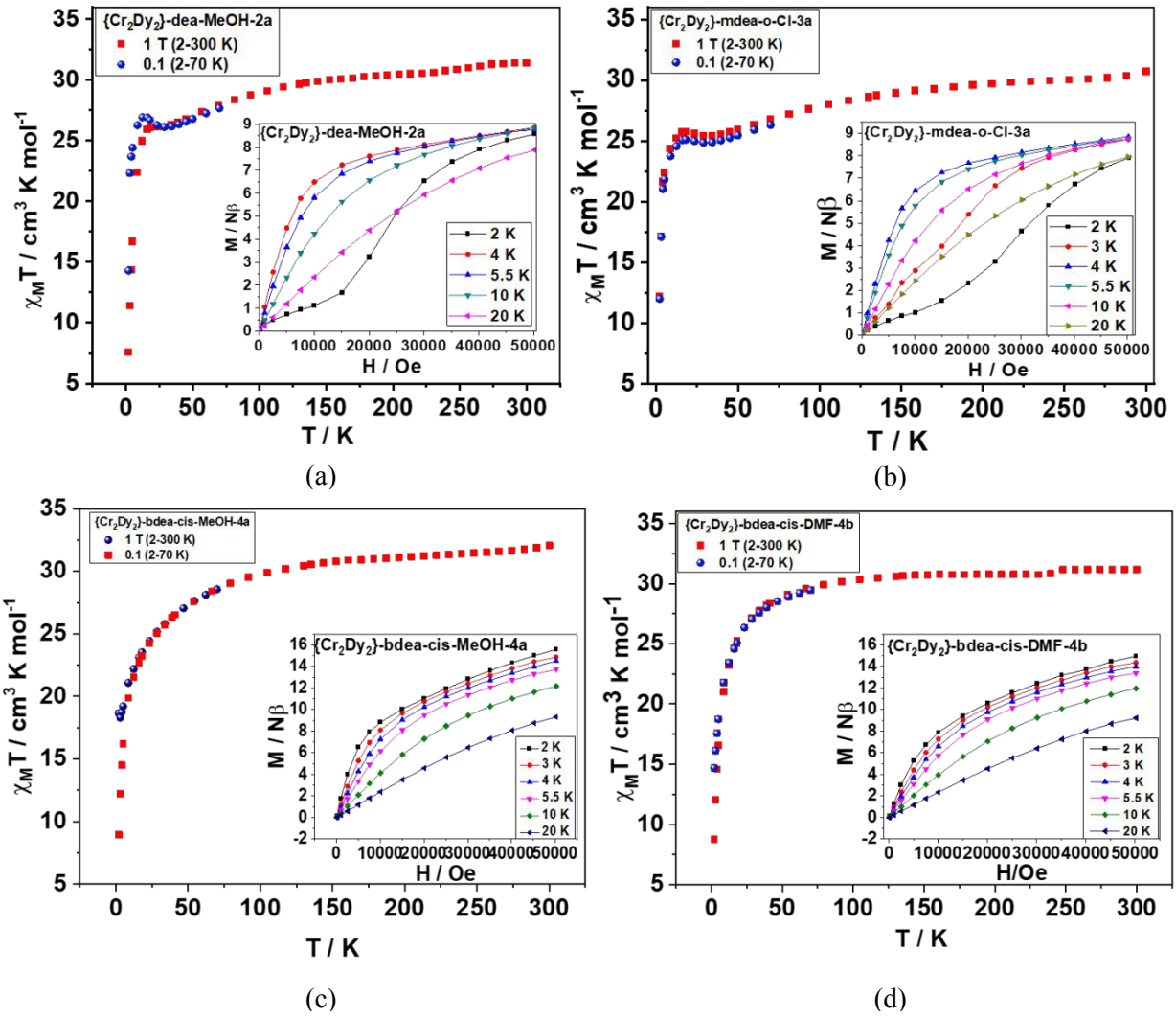

Figure **3**. The DC $\chi_M T$ vs T and M vs H isotherm (inset) plots for complexes **2a** (a), **3a** (b), **4a** (c) and **4b** (d).

Magnetic Properties

Direct current magnetic susceptibility measurements have been performed on powdered polycrystalline samples in the temperature range between 2 to 300 K under an applied field of 1 and 0.1 T. The $\chi_M T$ vs temperature plots are shown in Figure **3** for **2a**, **3a**, **4a** and **4b** and plots for the remaining molecules are shown in Figures **S3a-S3d**. The room temperature $\chi_M T$ value for each complex matches well with the calculated value for having two non-interacting Cr^{III} (S = 3/2, g = 2, C = 1.875 cm^3 K mol^{-1}) and two Dy^{III} (S = 5/2, L = 5, $^6H_{15/2}$, g = 4/3, C = 14.17 cm^3 K mol^{-1})

View Article Online
DOI: 10.1039/D4QI01484G

ions of 32.09 cm^3 K mol^{-1}. For complexes **2a-2d** and **3a-3g** the $\chi_M T$ behaviour closely resembles that of complex **1** measured in dc fields of 0.1 T and 1 T.[39] For example, for **2a** at 0.1 T, as the temperature decreases from 300 K, the $\chi_M T$ values decrease gradually until reaching ~ 30 K, then there is a small increase towards a maximum at ~12 K followed by a sharp drop below 12 K down to 2 K. In the 1 T measurement, there is a continuous drop in the $\chi_M T$ value till 50 K; then it drops and plateaus before a further decrease occurs at low temperature. The slight decrease in the $\chi_M T$ values at high temperatures is attributed to the depopulation of m_J levels of the Dy^{III} ions, whereas the increase/plateau below 50 K is due to the presence of non-negligible magnetic interaction between the Dy^{III}-Cr^{III} centers. As seen from Figures **3** and **S3a-3d**, we can see that the $\chi_M T$ values behave differently at low temperatures, and this is dependent on the nature of the exchange strength between the Dy^{III} and Cr^{III} centers; for each case, the behaviour is explained below, when discussing the theory of exchange.

For complexes **4a-4c**, the $\chi_M T$ values decrease continually from 300 K as the temperature is reduced, decreasing more rapidly below ~70 K (Figure **3**, bottom) with no increase or plateau. This behaviour is markedly different to that observed for **1**, **2a-2d** and **3a-3g.** For **4a**, however, a small rise is observed at very low temperatures (at 0.1 T), these differences are discussed below, *vide infra*.

The isothermal magnetisation curves for **1**, **2a-2d** and **3a–3g**, plotted against the dc magnetic field (inset Figure **3** and Figure **S3**), depict the presence of significant anisotropy for all the complexes. There is S-shaped behaviour in M when magnetised from zero field for the 2 K isotherms, which is indicative of hysteresis behaviour (see later). For **4a-4c,** this behaviour is absent, with an increase in M occurring at all temperatures without reaching saturation.

Due to the likelihood of SMM behaviour for **1, 2a-2d** and **3a-3g,** alternating current magnetic measurements have been made on the powdered samples of all the complexes. All complexes display SMM behaviour with frequency and temperature-dependent out-of-phase susceptibility peaks observed. Representative plots of the in-phase (χ_M') and out-of-phase (χ_M'') vs frequency (0.1 – 1500 Hz), Cole-Cole and ln(τ) vs $1/T$ show good resolution and are shown for **2b** in Figure **4**. At all temperatures studied (4.5 – 10 K), it was found that the relaxation is thermally activated, and plots of ln(τ) versus $1/T$ are linear, which suggests that an Orbach process is operative over the entire temperature and frequency range investigated. Fitting the data to the Arrhenius law [τ =

View Article Online
DOI: 10.1039/D4QI01484G

$\tau_o \exp(U_{eff}/k_B T)]$ yields an effective barrier to magnetisation reversal: U_{eff} = 79.1 K (ca. 54 cm^{-1}) with τ_o = 3.4 x 10^{-8} s (R=0.99) for **2b**. This relaxation behaviour is observed for all complexes **1, 2a-2d** and **3a-3g** and analysed in a similar manner, and the respective U_{eff} are provided in the Table **2**. The key observation for each complex is that even at the lowest temperatures, there is no crossover towards a QTM relaxation regime on the timescale of the ac experiment, which is extremely common for lanthanide-based SMMs. The U_{eff} and τ_o values for all the complexes are listed in Table **2**.

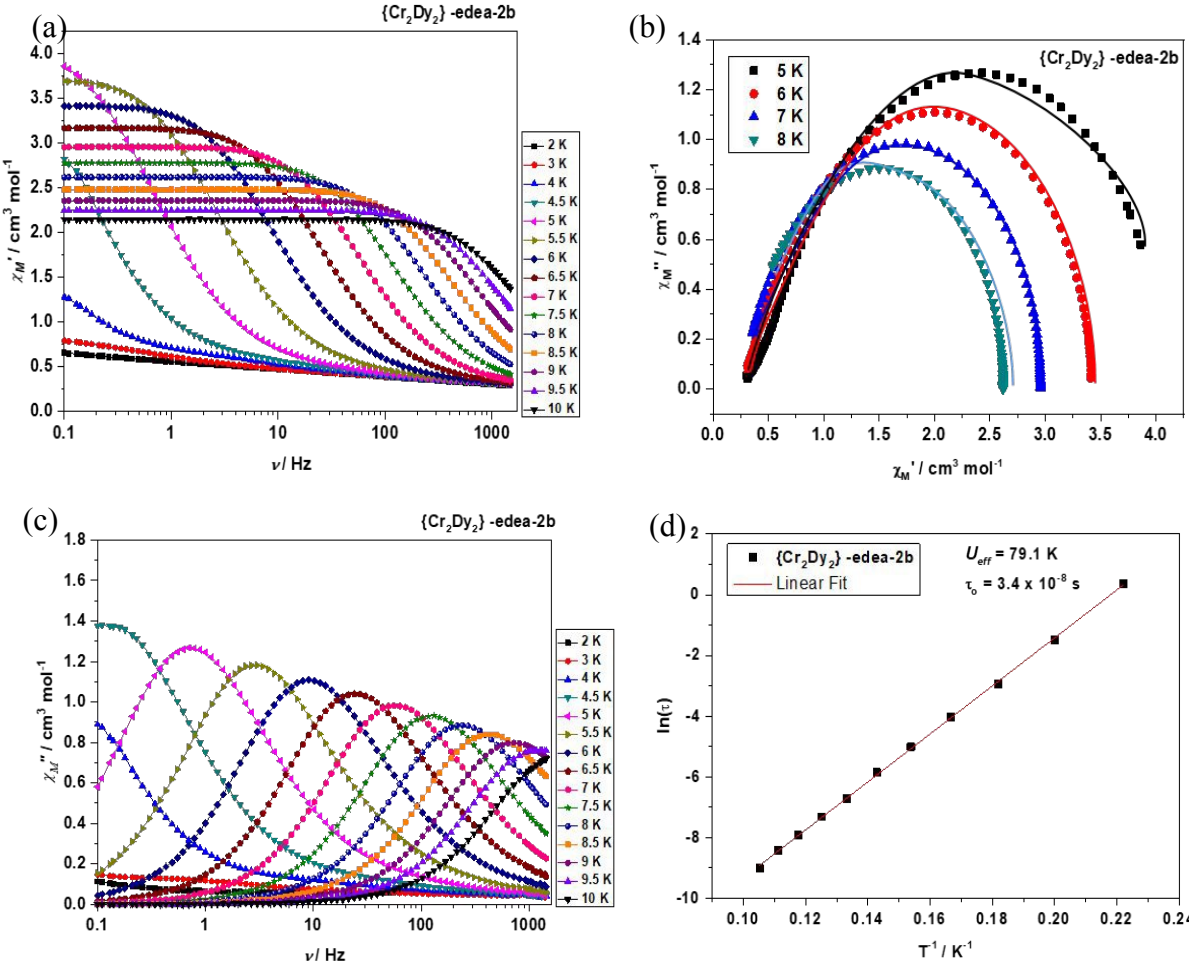

Figure **4**. Plots of in-phase (χ_M') and out-of-phase (χ_M'') vs. frequency (0.1 - 1500 Hz), Cole-Cole and ln(τ) vs.1/*T* for **2b**.

For **4a-4c**, the relaxation behaviour changes somewhat. Complexes **4b** and **4c** reveal no out-of-phase susceptibility signals above 1.8 K and, therefore, no SMM behaviour. For **4a**, however, frequency and temperature-dependent out-of-phase susceptibility signals are found between 2 –

View Article Online
DOI: 10.1039/D4QI01484G

6.5 K, following a similar profile to those shown above (Figure **S5a-5n**) however after performing an Arrhenius analysis on the relaxation rates, we find that U_{eff} = 32 K (τ_0 = 6.16 x 10^{-7} s), which is roughly half as big as seen in groups 1, 2 and 3.

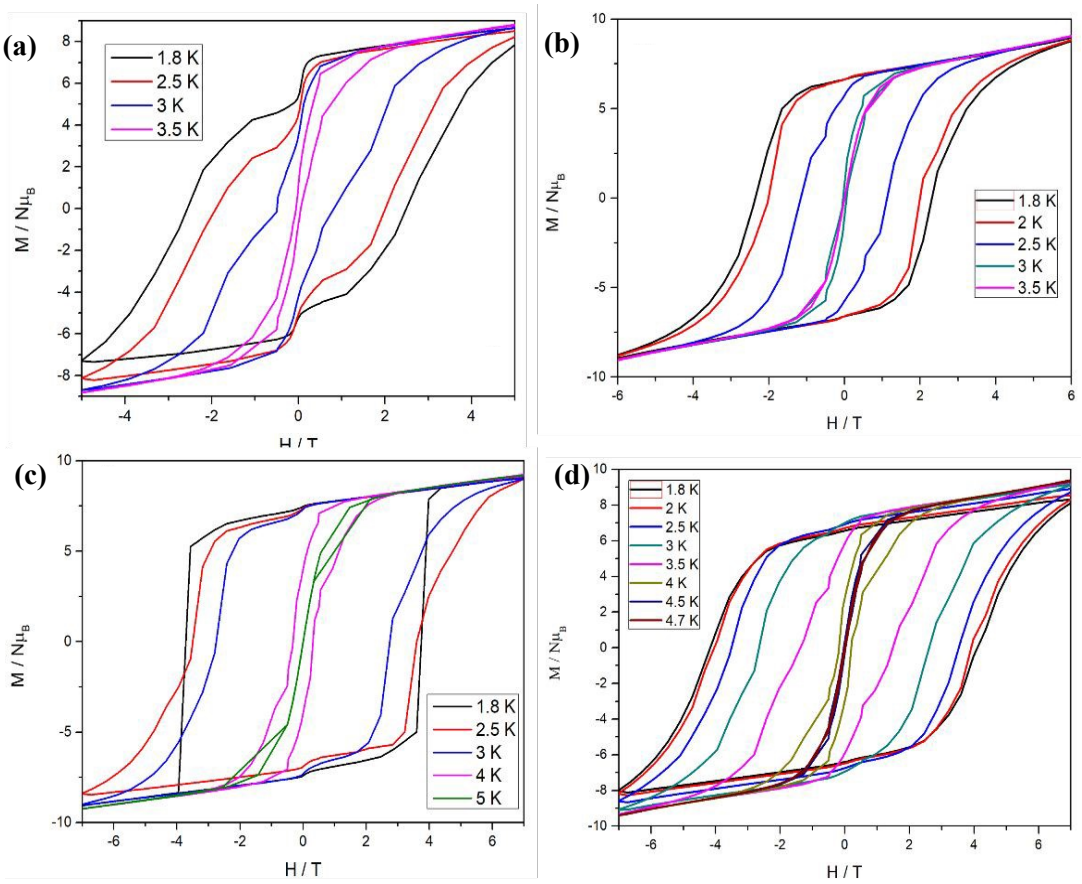

Figure **5**. Plot of magnetization (*M*) versus field (*H*) for (a) **1,** (b) **2c**, (c) **3c** and (d) **3d** sweeping the field with an average sweep rate of 0.003 T s^{-1}, at the temperatures indicated.

Because of the relatively large thermal barriers and lack of observable QTM, we performed variable-field magnetisation measurements to probe the relaxation dynamics over a longer time scale and search for magnetic hysteresis. It was found that using sweep rates accessible with a conventional magnetometer (an average of 0.003 T s^{-1}) on a polycrystalline sample, we were able to observe magnetic hysteresis for **1**, **2a-2d** and **3a-3g**. Hysteresis plots are shown for **1, 2c, 3c, and 3d** in Figure **5** (see Figures **S4a-b** for the remaining complexes). From the data, we can clearly see open magnetic hysteresis loops with large coercive fields. In some cases, we observed some loss of magnetisation at a zero field, indicating QTM, which was not apparent on the much faster time scale of the dynamic AC experiment. Interestingly, we find that the coercive field and

View Article Online
DOI: 10.1039/D4QI01484G

blocking temperature changes for each complex (Table **2**). This must be indicative of structural modifications for each complex. In order to understand these results, we have performed theoretical DFT/*ab initio* calculations, which will be discussed next.

Theoretical Studies

Ab initio calculations were performed on all complexes by taking the single crystal X-ray diffracted coordinates and employing the CASCCF/RASSI-SO/SINGLE_ANISO/POLY_ANISO module to obtain both the single-ion magnetic properties as well as the overall magnetic properties emanating from the exchanged coupled states. The computational methodologies are provided above in the

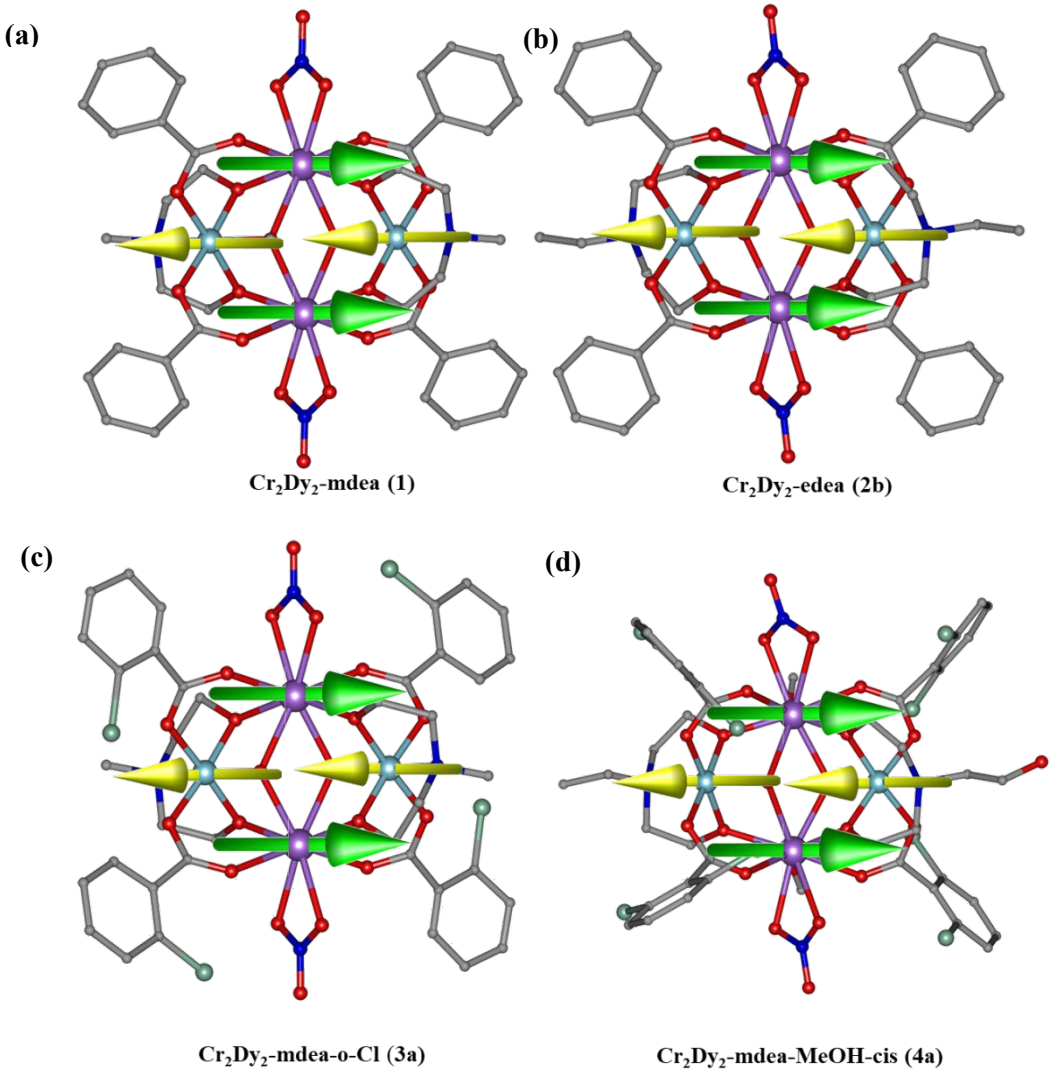

Figure **6**. The arrangement of the ground state anisotropic axis obtained from the POLY_ANISO module for the complexes **1**,[39] **2b**, **3a** and **4a**. Green arrows represent the Dy^{III} ions and the yellow arrows the Cr^{III} ions.

View Article Online
DOI: 10.1039/D4QI01484G

experimental section. For all complexes, the resulting single-ion magnetic properties, the low-lying Kramers doublets, along with the *g*-anisotropy are listed in the ESI Tables **S3-S4**.

Mechanism of Magnetization Relaxation for the Single-ion Dy^{III} centres: Employing the same level of basis set and methodologies for all fifteen complexes, including the starting complex **1**, their single-ion anisotropic properties have been compared. For all complexes, the ground and 1st excited state anisotropy are found to be axial in nature ($g_{zz} \sim 19.9$, $g_{xx} = g_{yy} \sim 0$), and the transverse component arises from the 2nd excited state (Table **S4**). The computed energy levels of the KDS (up to n+1 level with 'n' being the state via relaxation is facilitated) for all fifteen complexes are shown in Figure **7** (see also Table **S3** and Figure **S6** for the full energy level diagram).

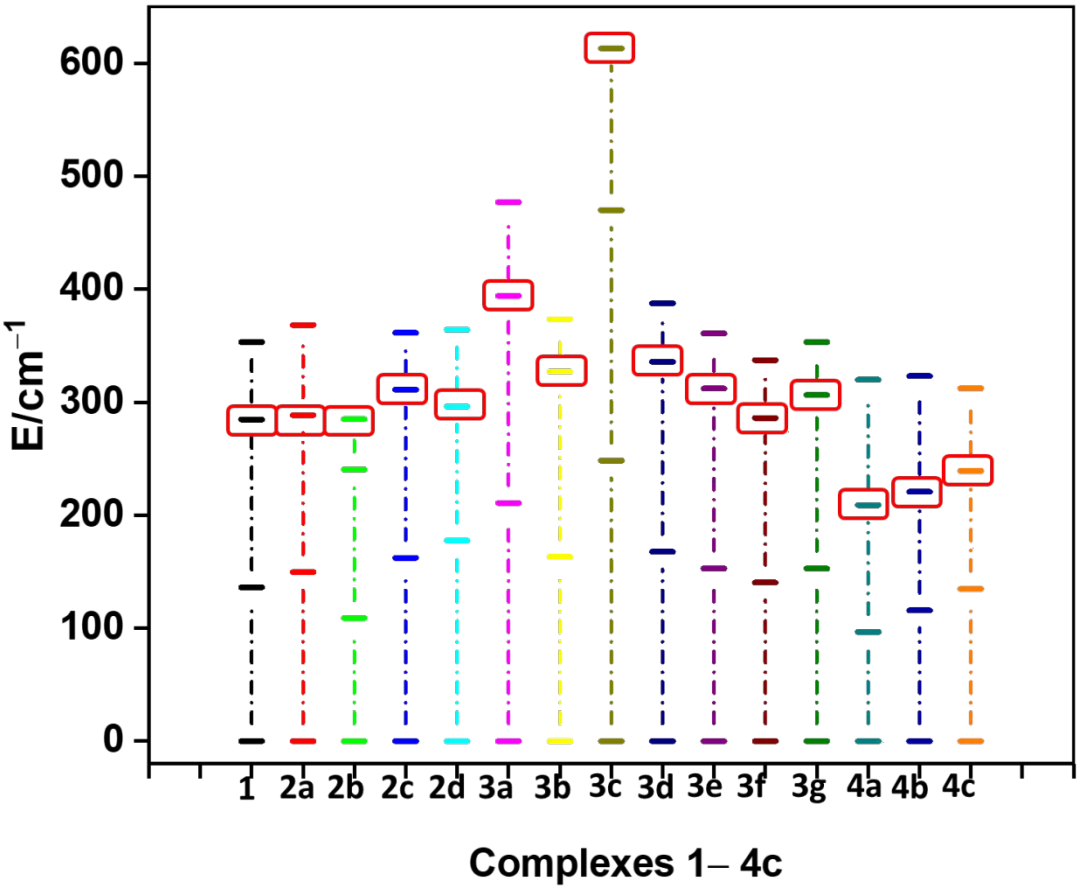

Figure 7. The energy distribution of low lying Kramers doublets for all the complexes. The red square indicates the state for magnetic relaxation originating from the single Dy^{III} centre.

Single-Ion Magnetic Anisotropy of 2a-2d: The structural changes in the substituted polyamine-alcohol have a large effect on the crystal field splitting, which is due to both the structural and electronic effects offered by the substituents on the polyamine-alcohols; however, the former plays

View Article Online
DOI: 10.1039/D4QI01484G

a dominant role as discussed below. It is interesting to note that increasing the size of the substituents from methyl to ethyl results in a decrease in the crystal field energy gap between the ground to the first excited state (136 cm^{-1} for **1** vs 109 cm^{-1} for **2b**) (Figure **7** and Table **S3**). However, in contrast, a bulkier substituent like the n-butyl group increases the energy splitting (136 cm^{-1} for **1** vs 162 cm^{-1} for **2c**) (Figure **7**, Table **S3**). For complex **2a** ($deaH_2$), an increase in the ground to 1st excited state energy (149 cm^{-1}) is found compared to **1** (136 cm^{-1}). The replacement of $(mdea)^{2-}$ to $(dea)^{2-}$ also changes the terminal coordination of the Dy^{III} ion; for complexes **1**, **2b** and **2c** a chelating nitrate group is coordinated to the Dy^{III} ion, whereas for **2a**, it is coordinated to two terminal MeOH groups. For complex **2d**, when $(mdea)^{2-}$ is replaced by $(teaH)^{2-}$, the ground to 1st excited state gap is found to be 177 cm^{-1}, the largest among this group of complexes. The ground state anisotropy axis derived from POLY_ANISO fitting for **1** and **2a-2d** for Dy^{III} ions are shown in Figure **6** and Figure **S1** and lie along the O-atoms of amine-polyalcohol groups (Figure **S1** and **S8**) and lie parallel to each other. The same is true for both the Cr^{III} centers, i.e. they lie parallel to each other (Figure **6** and Figure **S1**). However, the arrangement of the anisotropy axes of Dy^{III} and Cr^{III} are anti-parallel to each other, which has been obtained from POLY_ANISO fitting (Figure **6** and **S1**; *vide infra*).

To obtain a clearer picture of the structural vs electronic effects, i.e. whether the changes in the geometry around the Dy^{III} centre are due to different substitutions or are purely electronic in origin, we have modelled a similar complex to that of **1** by introducing a Cl group at the ortho position of the benzene ring (complex **1a**, which resembles complex **3a** Figure **S1**), however, keeping the bond parameters the same to that of **1**. The calculations yield a slight enhancement of the overall KD splitting (by ~1.95% see Table **S3**) and nearly identical *g*-anisotropy to that of complex **1**, however we find a substantial difference from complex **3a**. This emphasises the importance of structural alterations that occurs due to the change in the functional group (98% vs 2%) rather than the electronic structure of the functional group itself, as seen earlier in other systems.[66]

View Article Online
DOI: 10.1039/D4QI01484G

The magnetic relaxation dynamics were plotted for all complexes in Figure **8** (**2a**, **3a, 4a** and **4c**) and in Figure **S7**. In all cases, magnetic relaxation occurs via the 2nd excited state through TA-QTM/Orbach process. The U_{cal}^{Dy} from the single Dy^{III} ion *ab initio* calculations for **1**, **2a-2d** follows the order **2b** (240 cm^{-1}) < **1** (285 cm^{-1}) < **2a** (288 cm^{-1}) < **2d** (296 cm^{-1}) < **2c** (311 cm^{-1}). As shown in Figure **6** (Figure **S11**) the main anisotropy axis points towards the Dy–O bonds from the aminopolyalcohol ligands, thus a shorter Dy–O bond length would correspond to a stronger axial ligand field and hence a larger U_{cal}^{Dy}. The largest U_{cal}^{Dy} (**2c**) and smallest (**2b**) were found to correlate to the Dy–O bond length corresponding to the amine polyalcohol ligand (average 2.275

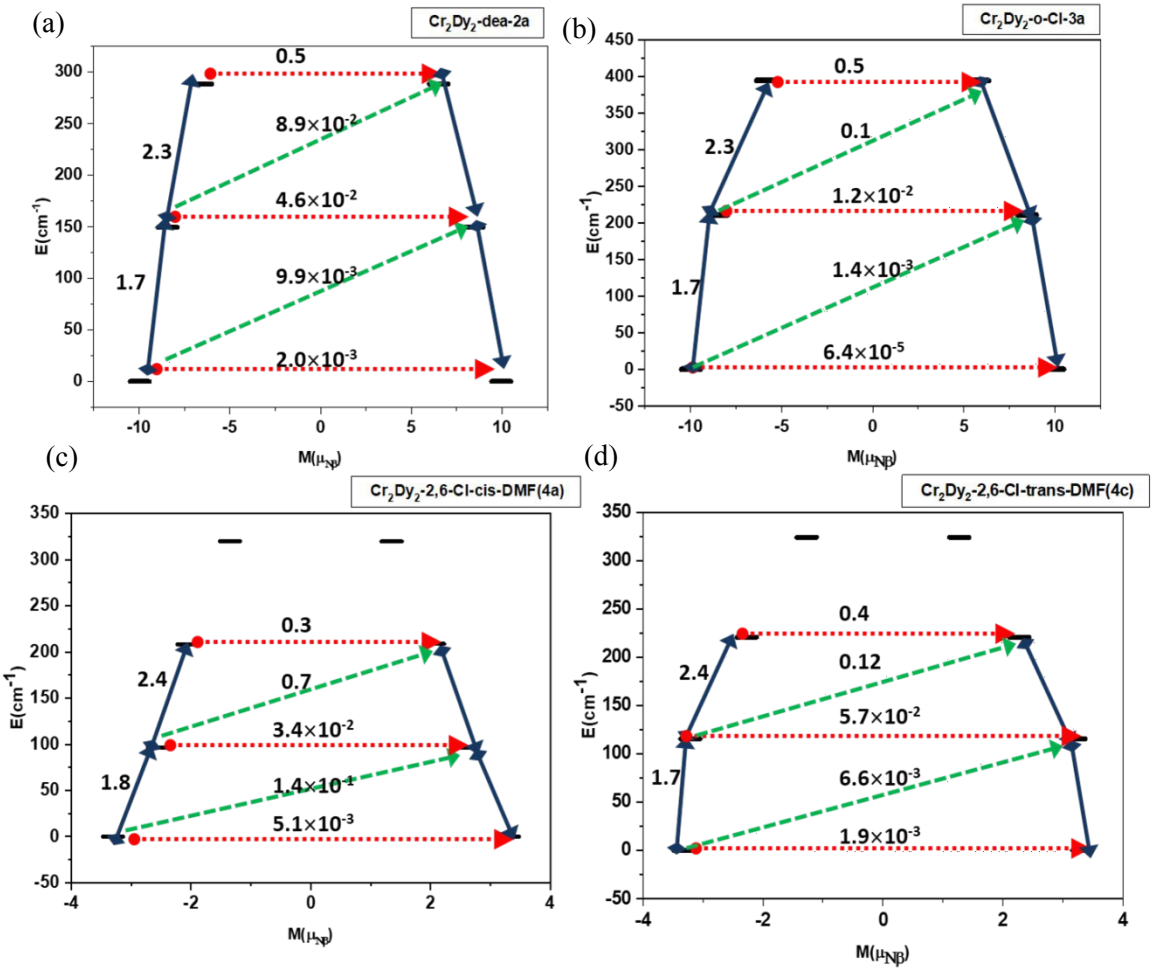

Figure **8**. The magnetic relaxation dynamics originating from the single Dy^{III} centre for **2a** (a), **3a** (b), **4a** (c) and **4b** (d). Red dotted line indicates QTM(TA-QTM), solid blue line for TA, Green line for Raman/Orbach Processes. Number above the line indicates the transition probabilities.

View Article Online
DOI: 10.1039/D4QI01484G

vs 2.243 Å for **2b** and **2c**, respectively, see Table **1**), with shorter distances yielding the largest U_{cal}^{Dy} and longer distances yielding the smallest U_{cal}^{Dy} in this family of complexes. The difference in distance observed is correlated to the electronic effect of the substituents, which alter the donor capability of the polyalcohol amine, which in turn is likely to change the donor nature of the oxygen arm. However, the bond length correlation does not hold true for the entire series, and neither is it found to correlate to the electronic nature of the substituents (inductive effects, etc.). This is essentially due to the minor variation in the bond length (of the order of ~0.03 Å), causing significant variation in the magnetic behaviour. This demands a quantitative analysis based on the computed charges, which are discussed below.

Single-Ion Magnetic Anisotropy of 3a-3g: For this group of complexes, we have modified the functional groups at the benzoate bridging ligand, which would alter the donor capability of the corresponding oxygen atoms, and this has been performed in three ways: (i) For **3a**, **3c**, **3d-3f** using $(mdea)^{2-}$ identical to **1** and alter the substituents around the aromatic ring of the benzoate ligand; (ii) For **3b** keeping the n-butyl group intact similar to **2c** and alter the 2, 6-positions of the benzoate ligand with -Cl; (iii) For **3g** employ a *tert*-butyl amine polyalcohol group along with *tert*-butyl substitution at the benzene ring. Thus **3b** and **3g** are expected to have mixed effects on both the functional groups, and a direct comparison or correlation to **1** is not possible. The ground and 1st excited state *g*-anisotropy are highly axial similar to **2a-2d**. The 2nd excited state shows some transverse components (see Table **S4**). The ground-to-first excited state energy gap for the KDs follows the ensuing order **3f** (140 cm^{-1}) < **3g** (152 cm^{-1}) < **3e** (153 cm^{-1}) < **3b** (163 cm^{-1}) < **3d** (167 cm^{-1}) < **3a** (211 cm^{-1}) < **3c** (248 cm^{-1}). For complexes **3a-3g**, the ground state anisotropic axis lies along the O-atom of the amine polyalcohol group (with a deviation of 10 – 20°, see Figure **S8**).

All of these complexes have a larger ground to 1st excited state energy gap compared to **1**. This is essentially due to the fact that the substitution at the benzoic position is expected to reduce the donation at the corresponding oxygen atom compared to the unsubstituted benzoate group in **1** (except for **3f** and **3g**, which increases the amount of electron density to the donor ligands). This reduction for the majority of complexes in the charge at the substituted benzoate oxygen atoms leads to weaker equatorial donation, which is known to destabilise the first excited KDs, leading to a larger gap (see Figure **S11**).

View Article Online
DOI: 10.1039/D4QI01484G

For complexes **3a-3g**, relaxation occurs via the 2nd excited state except **3c**, where it is predicted to occur via the 3rd excited state. The order of the computed U_{cal}^{Dy} values is found to follow the order **3g** (277 cm^{-1}) < **3f** (286 cm^{-1}) < **3e** (312 cm^{-1}) < **3b** (327 cm^{-1}) < **3d** (336 cm^{-1}) < **3a** (394 cm^{-1}) < **3c** (613 cm^{-1}) (Figure **8**, Figure **S6/S7** and Table **S3**). It is clear from these calculations that the introduction of an electron-donating group such as OMe (complex **3f**) at the ortho position or *tert*-Bu (complex **3g**) at the para position of the benzoate ring causes a smaller crystal field splitting, in accordance with the expected electron-donating capability of the substituent groups (**3f** being a better electron donor through the π system than **3g** through the σ donor system). Depending on the number and the position of the electron-withdrawing group, the ground-to-first-excited state gap varies for the other five complexes. If we compare the structures containing $(mdea)^{2-}$ as the amine polyalcohol (i.e. **3a**, **3c-3f**), the largest U_{cal}^{Dy} is found for **3c** while the smallest is found for **3f**. This is attributed to the fact that for **3c**, there are three -Cl groups substituted in the aromatic ring, offering a significant electron withdrawal effect, leading to a reduction in the donor capability of the corresponding oxygen compared to the $(OMe)^-$ group in **3f** which enhances the donor strength of the equatorial oxygen. This is clearly reflected in the Dy–O bond distance, with a longer Dy–O bond found for **3c** and a shorter one found for **3f** (2.414 Å vs 2.340 Å). As this oxygen lies in the equatorial position, lengthening of the bond leads to a larger U_{cal}^{Dy} value and *vice-versa*. These effects are also reflected in the computed LoProp charges[82] for the corresponding oxygen atoms (–0.668 vs –0.723) for the O atoms of **3c** and **3f**, respectively (see Figures **S10-S11)**.

From the above analysis, it is clear, again, that the electronic factors of the substituents slightly alter the bond geometries, which has a consequential effect on the computed magnetic properties. For complexes **1**, **2a-2d,** and **3a-3g,** which have eight oxygen donor atoms with a $\{DyO_8\}$ core, out of the eight O-atoms, two of the axial O-atoms from the aminepolyalcohol group and two of the equatorial O-atoms from the $(NO_3)^-$ group (or MeOH for **2a**) is primarily determining the strength of KDs energy splitting and hence the U_{cal}^{Dy} values. Another factor contributing to the difference in the observed U_{cal}^{Dy} values for these complexes are the amount of deformation of the $\{DyO_8\}$ core. This was indeed reflected in the observed LoProp charges on the surrounding O atoms and, hence on the crystal field parameters, leading to the largest observed U_{cal}^{Dy} values from the single Dy^{III} center for **3c**. The variation of the ground to 1st excited state energy splitting with respect to the difference in the percentage of axial and equatorial LoProp by taking the equal

View Article Online
DOI: 10.1039/D4QI01484G

contribution of charges has been plotted in Figure **9** (the difference of axial and equatorial LoProp charges/total charge x 100), and the detailed LoProp charge around each O-atom has been provided in Figure **S10-S11** in ESI for all the complexes. It has been noticed that a pseudo linear or sinusoidal correlation exists between the difference of axial to equatorial LoProp charge and the computed ground to 1st excited energy gap exist. The pseudo linear or sinusoidal behavior can be attributed to the fact that all these complexes are not completelystructurally analogous to each other due to the wide variety of ligand systems (categories 1 to 3) having been employed. This reflects on the axial crystal field parameters B_2^0 obtained from the Hamiltonian provided in equation **S1** in the ESI (H_{CF}); a larger magnitude in B_2^0 indicates a large axial approach of the ligand field, and the splitting between the low-lying KDs increases.[83] For all the studied molecules, the crystal field parameters have been provided in Table **S6** of the ESI.

Single-Ion Magnetic Anisotropy of 4a-4c: For the last set of complexes **4a-4c**, there is an extra coordination site attached to the Dy^{III} ions, and therefore the Dy^{III} ion is nine coordinate with a $\{DyO_9\}$ motif. For all three complexes, the carboxylate is 2,6-dichlorobenzoate, which is the same as for complex **3b**, with the amine polyalcohol ligands being $(teaH)^{2-}$ (**4a**), $(bdea)^{2-}$ (**4b**) and $(mdea)^{2-}$ (**4c**). For complex **4a**, along with the chelating $(NO_3)^-$, a MeOH is coordinated to each Dy^{III} ion. The MeOH ligands lie *cis* to each other. For complexes **4b** and **4c**, a chelating nitrate is present with a terminal DMF ligand at each Dy^{III} ion, that lies *cis* and *trans* to each other, respectively. We find that despite moving from eight to nine coordinate environments, there is minimal change in the ground, 1st and 2nd excited g-anisotropy values (Table **S4**); however, in comparison to the other complexes, the ground to 1st excited gap is reduced (Figure **7** and Table **S3**), and smaller U_{cal}^{Dy} values are found - 249 cm^{-1}, 220 cm^{-1} and 208 cm^{-1} for **4a**, **4b** and **4c**, respectively. The significant reduction in the ground-first excited state gap and the U_{cal}^{Dy} value compared to groups **1**, **2** and **3** are due to the additional ligand. For **4a** the extra MeOH ligand is found equatorial to the anisotropy axis, thus reducing the ground to 1st excited state gap. For **4b** and **4c**, however, the extra coordinated DMF ligand alters the position of one of the O–atoms of the polyalcohol ligand to lie equatorial compared to the other complexes where both the oxygen atoms lie along the axial direction (Figure **S11**). As these two amine polyalcohol O–atoms provide the shortest bond length and the strongest ligand field, moving one of the O–atoms to an equatorial position destabilises the first and second excited states leading to a drastic reduction in the U_{cal}^{Dy}

View Article Online
DOI: 10.1039/D4QI01484G

value. Furthermore, as the geometry around the Dy^{III} ion changes from a pseudo D_{4d} square antiprismatic geometry, which is favoured for Dy^{III} SMMs, the tunnelling contribution at the ground and excited states are larger (1.1×10^{-3} for **3b** vs 5.1×10^{-3} for **4b**) leading to the suggestion of the absence of single-ion magnetic relaxation for this set of complexes.

The single aniso calculations indicate the axial approach of the ligand field and, hence, the contribution towards the overall energy barrier for magnetic relaxation. For the majority of complexes, the calculations predict good SMM behaviour, and this is found to be the case experimentally. The calculations also indicate the absence of SMM behaviour for **4b** and **4c**, which is also the case. The experimentally observed U_{eff} barrier in each molecule is, however, substantially less compared to the single ion-derived values (Table **2**). Furthermore, there is no direct linear correlation between the observed U_{cal}^{Dy} and the experimental U_{eff} (see Figure **S12**). As it was revealed from complex **1** that there is a significant magnetic exchange interaction between the Dy^{III}–Cr^{III} ions, and the overall magnetic relaxation is strongly dependent on the exchanged coupled states, we, therefore, probe the influence of the exchange coupling on the SMM behaviour.

Mechanism of Magnetization Relaxation for the {$Cr^{III}_2Dy^{III}_2$} motif:

To estimate the exchange coupling in these $\{Cr^{III}_2Dy^{III}_2\}$ complexes, the following Hamiltonian was employed

$$H = -J_{Dy-Dy'}[S_{Dy,Z}S_{Dy',Z}] - J_{Dy-Cr}[S_{Dy,Z}S_{Cr} + S_{Dy',Z}S_{Cr'}] - J_{Dy-Cr'}[S_{Dy,Z}S_{Cr'} + S_{Dy',Z}S_{Cr}] - J_{Cr-Cr}[S_{Cr1}S_{Cr2}] \quad \text{Eqn (2)}$$

The dipolar contribution to the magnetic exchange was computed using the dipolar Hamiltonian which is shown in equation **S2**. There are three different exchange interactions that exist in these metal cores, which are between the Dy^{III}–Dy^{III}, Dy^{III}–Cr^{III} and Cr^{III}–Cr^{III} ions. In each molecule, there are six exchange pathways present, one between Cr^{III}–Cr^{III}, one between Dy^{III}–Dy^{III} and four between Dy^{III}–Cr^{III} (Figure **10a**). For the molecules where both the Dy^{III} and Cr^{III} centres are completely equivalent and can be attained by a 180˚ rotation, an equal value of $J_{Dy\text{-}Cr}$ and $J_{Dy'\text{-}Cr'}$ is expected, whereas when they are not exactly equivalent, two different J values have been estimated (for complexes **2b**, **4a** and **4c**).

View Article Online
DOI: 10.1039/D4QI01484G

The *J* values obtained from BS-DFT calculations using both Gaussian (B3LYP/TZVP) and Orca packages are provided in Table **2** and Table **S5** (DFT spin density plots shown in Figure **S13)**. For the Gaussian calculations, all six exchange interactions are taken into account simultaneously, whereas, for the ORCA calculations, the individual exchange terms between two paramagnetic centres have been calculated by substituting the other two centres with the diamagnetic metal centres, using the Hamiltonian provided in equation **1**. The fitted value using the POLY_ANISO module also follows the same Hamiltonian as equation **1**. The fitted values are provided in Table **2** along with the computed values (see Figure **S16** for the fitted $\chi_M T$ vs T data).

In all the cases, the nature of the exchange between the Cr^{III} and Dy^{III} ions is antiferromagnetic in nature. This is due to the significant overlap of the 4f orbital (all seven 4f orbitals) of the lanthanide with the 3d orbitals of Cr^{III} (d_{xy}, d_{yz} and d_{xz}) (Figure **10b**, $S_{ij} \sim 10^{-2}$ for $4f_{xyz}$ with $3d_{xy}$). Further, as the unpaired electrons for the Cr^{III} ions are in the t_{2g} orbitals, they are less efficient in charge transfer to the 5d orbitals of the Dy^{III}, which is established to be the primary contributor to the ferromagnetic part of the exchange.[84, 85] Thus strong antiferromagnetic contributions and weaker ferromagnetic contributions lead to overall antiferromagnetic exchange. For all systems, the $J_{Dy\text{-}Dy'}$ exchange is ferromagnetic in nature and is found to be in the range of 0.01 – 0.04 cm^{-1}. This is

View Article Online
DOI: 10.1039/D4QI01484G

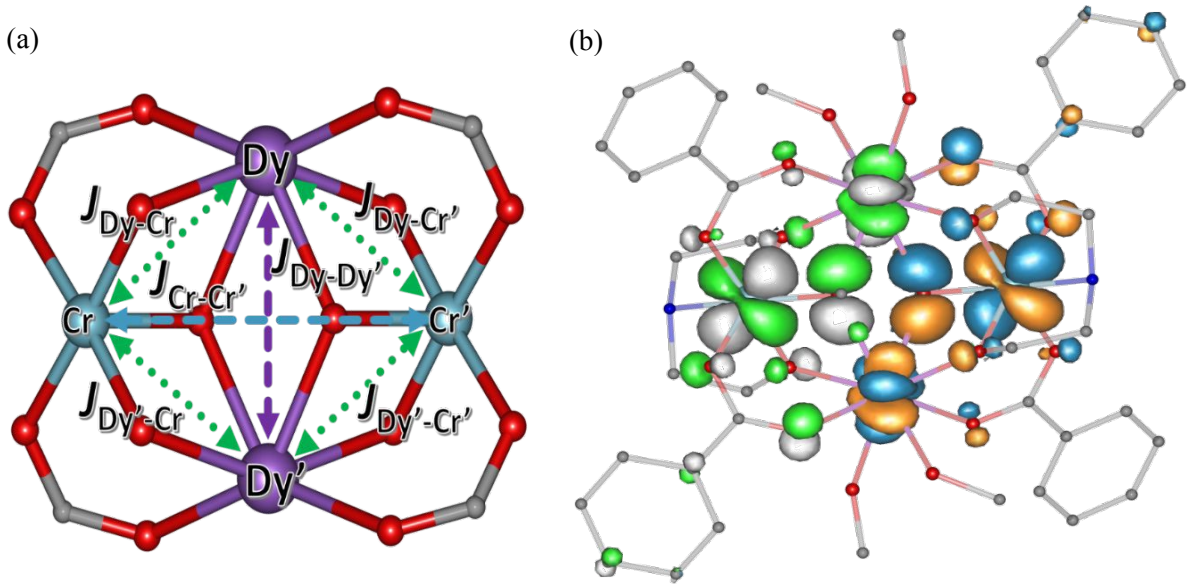

Figure **10**. (a) Mode of exchange coupling between the metal-metal centers in all the complexes. (b) the overlap between the 4f orbital of the lanthanide and the 3d orbitals of the Cr ion via the oxo bridges. The orange and blue lobes represent the α and β electron density for in the HS state and the green and gray lobes represents the α and β electron density in the BS states obtained from the density functional calculations.

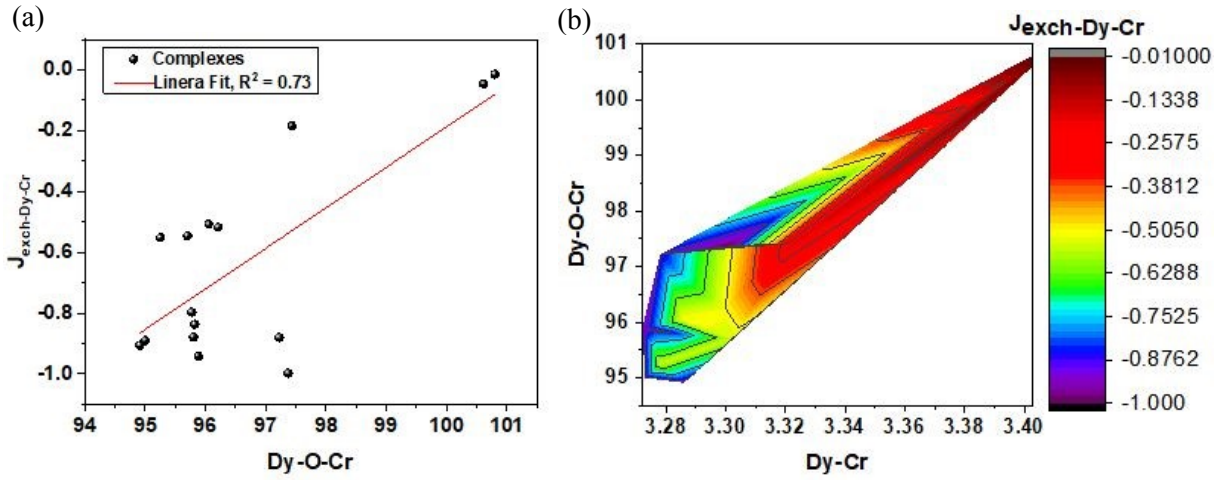

Figure **11**. Variation of $J_{exch-Dy-Cr}$ with respect to the Dy-O-Cr bond angle (a) and the variation of $J_{exch-Dy-Cr}$ with respect to both Dy-Cr bond length and Dy-O-Cr bond angle represented in a 3D plot (b).

View Article Online
DOI: 10.1039/D4QI01484G

essentially correlated to the fact that the super-exchange mediates via two μ_3 $(OR)^-$ groups with relatively acute Dy–O–Dy angles enforced by the butterfly geometry. For this angle, the exchange is expected to be ferromagnetic as per the earlier magneto-structural correlation established, affirming the computed data.[86, 87] The $J_{Dy\text{-}Cr}$ exchange for groups **1**, **2a-2d**, **3a-3g**, lie in the range of ~ –0.47 to –1 cm^{-1} (Table **2**). The largest $J_{Dy\text{-}Cr}$ exchange is observed for the **3a-3g** series,

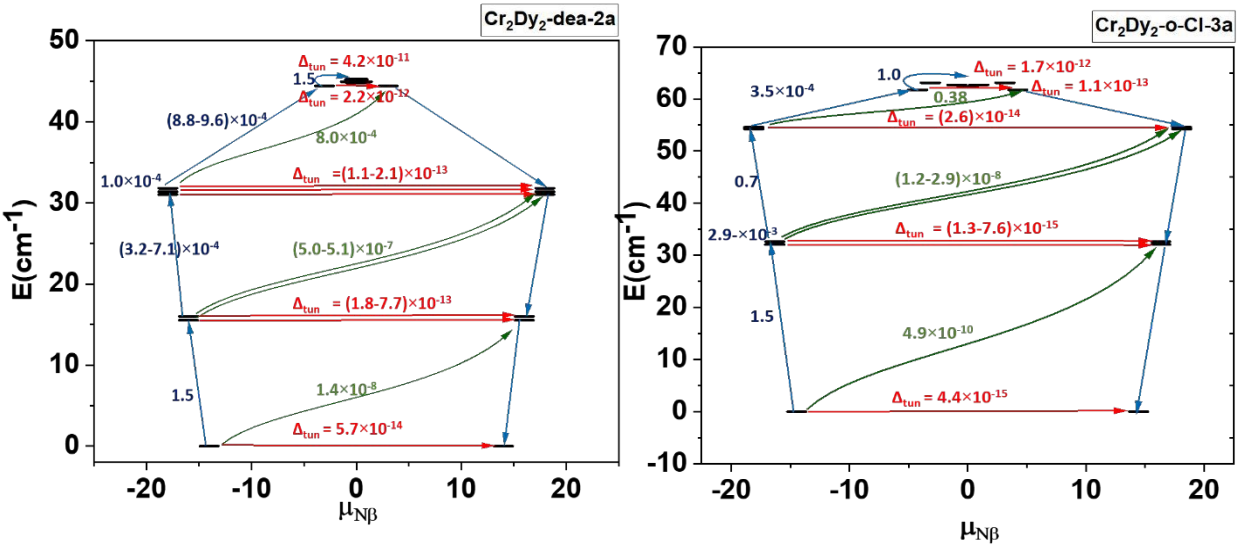

Figure **12**. Poly_Aniso computed U_{eff} barrier heights for complexes **2a** and **3a**.

followed by the **2a-2d**. The smallest $J_{Dy\text{-}Cr}$ exchange is found for **4a-4c** and lies in the range –0.05 – 0.57 cm^{-1}. These results correlate to the Dy–O bond lengths as well as the Dy^{III}–O_{amine}–Cr^{III} bond angles, which play a dominant role in determining the strength of magnetic exchange. A comparatively larger $J_{Dy\text{-}Cr}$ exchange has been noticed for complexes **3c-3g**, an intermediate-range for **1**, **2a-2d** and **3a-3b** and a much smaller exchange for **4a-4c**. This is due to the larger orbital overlap between the 4f orbitals of Dy^{III} ion with the p orbitals of the bridging μ_3–O, the carboxylate O–atom and the polyamine alcohol O–atom and the 3d orbital of the Cr^{III} ion for **3c-3g** (spin density on the oxygen 0.029–0.030, Figure **S11**) compared to the smaller overlap for the rest of the complexes. For **4a-4c**, the $J_{Dy\text{-}Cr}$ exchange is comparatively less (spin density on the oxygen 0.017 to 0.019**)** due to the increased bond length (average Dy–O 2.41 Å for **4a-4c** and 2.36 to 2.38 Å for the eight coordinated complexes). The variation of $J_{Dy\text{-}Cr}$ with respect to the Dy^{III}–Cr^{III} bond length and the Dy^{III}–O_{amine}–Cr^{III} angle has been plotted in Figures **11** and Figures **S13, S14** and **S18**. The Dy–O–Cr angle yields a quasi-linear regression suggesting that a larger Dy–O–Cr angle

View Article Online
DOI: 10.1039/D4QI01484G

leads to ferromagnetic $J_{Dy\text{-}Cr}$ exchange, while a smaller angle leads to antiferromagnetic exchange, though the Dy…Cr distance was also found to play a role in influencing the magnitude of the *J* value when the exchange gets strongly antiferromagnetic. In the weak antiferromagnetic region, *J* is found to be insensitive to the Dy….Cr distance (see Figure **11b**). Except for **4b** and **4c**, for the rest of the complexes, the $J_{Cr\text{-}Cr}$ is found to be ferromagnetic in nature and lies in the range of +0.04 to +0.28 cm^{-1}. This interaction is very weak, as expected, as these are next-nearest-neighbour interactions, and the magnitude of the computed *Js* are found to be correlated to various geometric parameters, with the Cr…Cr distance being the prominent one. It also appears that the nature of Cr^{III}–Cr^{III} exchange influences the U_{eff} and T_B along with the Cr^{III}–Dy^{III} exchange (see below). At low temperatures, this effect plays a dominant role and is observed experimentally in the $\chi_M T$ vs *T* plots, hence quenching QTM and leading to SMM behaviour at zero field. Interestingly, this is further corroborated, as shown for complexes **4b** and **4c**, where an antiferromagnetic $J_{Cr\text{-}Cr}$ leads to the absence of SMM behaviour. Very recently, Rentschler and co-workers reported a similar $\{Cr^{III}_2Dy^{III}_2\}$ butterfly complex, where the two Dy^{III} centres were replaced by two Y^{III} centres and revealed a ferro-magnetic Cr^{III}–Cr^{III} interaction with hysteresis observed.[88] For all fourteen complexes, the superexchange is relatively weaker than the dipolar interactions; however, they cannot be ignored. Including the superexchange along with the dipolar contribution is found to be crucial for reproducing the computed effective energy barrier from POLY_ANISO simulations in a way that aligns with experimental results. Further, the fits were found to be poor when exchange coupling interactions are excluded, suggesting that both contributions are crucial for their performance.

Table **2**. DFT computed J_{exch} and the *ab initio* fitted J_{tot}/J_{dip} parameters for all the complexes.

Complex	Gaussian J_{exch} BS-DFT			MOLCAS_Fitted			U_{eff}/ K	τ_o / s	T_B / K	H_c *(1.8 K) / T*
	$J_{Dy\text{-}Cr}$ $J_{Dy\text{-}Cr'}$	$J_{Dy\text{-}Dy}$	$J_{Cr\text{-}Cr}$	$J_{tot Dy\text{-}Cr}$ ($J_{dip Dy\text{-}Cr}$)	$J_{tot Dy\text{-}Dy}$ ($J_{dip Dy\text{-}Dy}$)	$J_{tot Cr\text{-}Cr}$ ($J_{dip Cr\text{-}Cr}$)				
1	-0.88/ -0.78	+0.03	+0.08	-4.0/-3.2 (-3.22/-2.32)	0.04 (0.07)	0.10 (0.02)	76	5.1 x 10^{-8}	3.7	2.7
2a	-0.52/ -0.80	+0.01	+0.04	-3.1/-3.15 (-2.30/-2.63)	0.03 (0.02)	0.06 (0.02)	60	2.3 x 10^{-7}	3.5	2.1

View Article Online
DOI: 10.1039/D4QI01484G

2b	-1.0/ -0.70	+0.01	+0.06	-3.75/-3.80 (-2.80/-3.12)	0.02 (0.01)	0.04 (0.03)	77	3.4 x 10^{-8}	4	2.5
2c	-0.80/ -0.86	+0.01	+0.07	-3.40/-3.50 (-2.54/-2.64)	0.02 (0.01)	0.03 (-0.04)	60	1.1 x 10^{-7}	3.5	2.4
2d	-0.51/ -0.70	+0.01	+0.04	-2.90/-2.90 (-2.39/-2.20)	0.02 (-0.07)	0.03 (-0.01)	62	8.3 x 10^{-7}	3.5	2.4
3a	-0.55/ -0.76	+0.01	+0.16	-4.25/-4.30 (-3.47/-3.75)	0.02 (0.01)	0.04 (-0.12)	85	4.8 x 10^{-8}	3.5	No data
3b	-0.55/ -0.47	+0.01	+0.28	-4.20/-4.30 (-3.65/-3.83)	0.02 (0.01)	0.32 (0.04)	84	8.6 x 10^{-8}	3.3	4.1
3c	-0.91/ -0.75	+0.01	+0.18	-4.40/-4.50 (-3.49/-3.75)	0.02 (0.01)	0.24 (0.06)	91	1.2 x 10^{-7}	4.5	3.8
3d	-0.98/ -0.89	+0.01	+0.16	-4.10/-4.10 (-3.12/-3.21)	0.02 (0.01)	0.18 (0.02)	85	5.1 x 10^{-8}	4.7	4.2
3e	-0.95/ -0.84	+0.01	+0.08	-3.90/-3.90 (-2.95/-3.06)	0.04 (0.03)	0.20 (0.12)	83	2.1 x 10^{-7}	4.5	3.1
3f	-0.94/ -0.84	+0.03	+0.08	-3.80/-3.95 (-2.86/-3.11)	0.02 (0.05)	0.10 (0.02)	77	5.6 x 10^{-8}	4	2.3
3g	-0.88/ -0.78	+0.03	+0.08	-3.10/-3.25 (-2.22/-2.47)	0.01 (0.04)	0.04 (-0.04)	63	3.8 x 10^{-8}	3.1	2.2
4a	-0.18/ -0.57/ -0.45	+0.04	+0.11	-1.80/-1.90 (-1.33/-1.75)	0.02 (-0.02)	-0.02 (-0.09)	32	5.9 x 10^{-7}	1.8	
4b	-0.27/ -0.12	+0.01	-0.22	--	--	--	n/a			
4c	-0.15 -0.05	+0.00 4	-0.10	--	--	--	n/a			

- A total of four different exchanges values are given for $\boldsymbol{J_{totDy\text{-}Cr}}$ (two of them are in parenthesis for $\boldsymbol{J_{dipDy\text{-}Cr}}$). Since both the Dy(III) and Cr(III) centers are not equivalent to each other, they are resulting in different $\boldsymbol{J_{totDy\text{-}Cr}}$ exchange values, the same is applicable for dipolar exchange as well ($\boldsymbol{J_{dipDy\text{-}Cr}}$) provided in the parenthesis

In all cases a nearly identical U_{eff} barrier has been derived using the POLY_ANISO module to that of the experimentally reported values (Figure **12)**. With the low-lying doublet states, the resulting exchange spectrum is depicted in Figure **12** and Figure **S17**. Each doublet's very modest tunnel

View Article Online
DOI: 10.1039/D4QI01484G

splitting effectively suppresses the ground state and thermally assisted QTM (represented by the number on the top of each arrow). Therefore, it is anticipated that the excited states shown by the blue arrows in Figure **12** will lead to the relaxation of magnetisation via a spin-phonon mechanism.

The relaxation path can be defined by connecting exchange states with the biggest transition magnetic moments, according to a recent proposal (blue numbers in Figure **12**).[89]

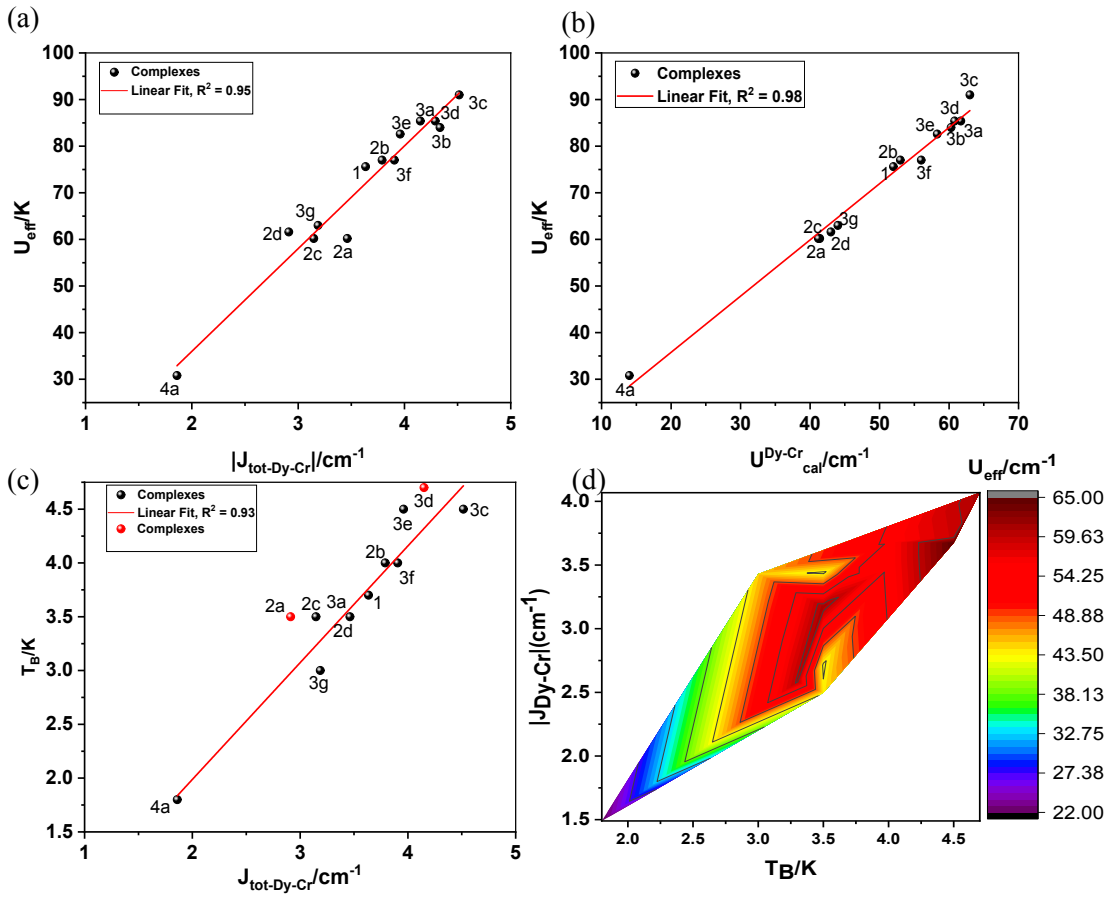

Figure **13**. (a) Variation of $J_{\text{tot-Dy-Cr}}$ vs U_{eff}, (b) $U_{cal}{}^{Dy\text{-}Cr}$ vs U_{eff}, (c) $J_{\text{tot-Dy-Cr}}$ vs T_B and (3d) dependence of U_{eff} and T_B on $J_{\text{tot-Dy-Cr}}$ represented in a 3D plot.

The calculated $U_{cal}{}^{Dy\text{-}Cr}$ for the entire system by considering the exchanged coupled states has been plotted against the U_{eff} values, which gives a good linear fit (Figure **13b**). The magnitude of J_{tot} is plotted with respect to the observed U_{eff} and shows a linear correlation between exchange parameters and the observed U_{eff}. The relationship of J_{tot} vs T_B also holds true with a linear relationship between the J_{tot} and T_B (figure **13c**). The variation of the magnitude of total magnetic

View Article Online
DOI: 10.1039/D4QI01484G

exchange, T_B and the observed U_{eff} values has been plotted in Figure **13d**, which indicates a stronger exchange is playing a dominant role in achieving large T_B and U_{eff} values. For complexes **1**, **2a-2d** and **3a-3g**, a large dipolar coupling has been observed and, hence a large J_{tot}. The largest J_{tot} is found for **3a-3d**, followed by **3e-3g** and **2a-2d**. Complex **2b** is found to have the largest J_{tot} among **2a-2d**. This is essentially reflected in the SMM behavior for all these complexes. A linear relation between the J values with U_{eff} and T_B, holds true throughout the series of complexes. We show that the POLY_ANISO simulations help in the extraction of the barrier for magnetic relaxation (U_{eff}) for all these complexes, aligning with the experimentally obtained values. However, predicting the T_B values from the exchange-coupled state is challenging, as T_B is influenced by spin-phonon effects, hyperfine coupling, and inter-molecular interactions. However, it can be proposed that the observed hysteresis may result from the low-lying exchange-coupled states; as the overall total exchange (J_{tot}) is similar to the observed blocking temperatures ($T_B \sim J_{tot}$). While the correlation between the two factors is evident from the provided data, the reason for such a correlation, beyond the quenching of QTM at zero-field and exchange-bias effects, remains unclear. This warrants further study to improve the T_B in this class of molecules.

Conclusion

In summary, synthesis, characterisation and magnetic properties, along with detailed theoretical analysis, have been performed for fourteen $\{Cr^{III}_2Dy^{III}_2\}$ butterfly complexes. Of the fourteen studied complexes, twelve were found to display SMM behaviour, and eleven revealed magnetic hysteresis above 3 K to 4.7 K with large coercive fields. These complexes are found to be some of the best 3d–4f SMMs reported. Various aspects have been explored in detail by computational methods in order to understand the magnetisation dynamics for these complexes. From the detailed experimental results combined with the theoretical studies, it has been revealed that;

a) The crystal field splitting and the exchange coupling strongly originate from the structural parameters as compared to the electronic effects. Depending on the nature and bulkiness of the substituents, the bond parameters and geometry around the metal centres differ strongly, leading to different crystal field splitting as the axial approach of the ligand changes. In all of the above complexes, the ground state anisotropy axis lies along the oxygen of the polyamine-alcohol group, whereas the oxygen of $(NO_3)^-$ (in some cases MeOH) lies in the equatorial plane. Substitution of various functional groups at various positions affects the Dy-O bond length and, hence the LoProp

View Article Online
DOI: 10.1039/D4QI01484G

charges on the respective oxygens. Depending upon the magnitude of these LoProp charges on the oxygens, the ground to 1st excited energy gaps determine the overall U_{Dy}^{cal} values.

b) The nature of the $J_{Cr\text{-}Cr}$ coupling plays a crucial role in determining the SMM behaviour for all complexes along with the magnitude of the $J_{Dy\text{-}Cr}$ coupling. The single-ion calculated U_{cal}^{Dy} parameter indicates that all complexes are SMM at a single-ion level. However, complexes **2a-2d**, **3a-3g** shows SMM behaviour with a significant T_B value. A detailed mechanism of magnetisation relaxation developed reveals that whenever the $J_{Cr\text{-}Cr}$ exchange coupling is ferromagnetic, this results in the observation of SMM behaviour, and if it is antiferromagnetic (as in the case of **4b-4c)**, it lacks SMM characteristics.

c) Depending on the bulkiness of the substituent, the bond angle between the Cr–O–Dy, and Dy–O–Dy changes, leading to different extents of orbital overlaps and, hence different exchange values with the angles playing a prominent role compared to other parameters in controlling the magnetic exchange. Quite interestingly, a near linear correlation between the T_B values and $|J_{Dy\text{-}Cr}|$ value was detected among the fourteen complexes reported suggesting that this particular exchange interaction is crucial in dictating not only the U_{eff} value but also T_B values.

d) Structural alterations that aim to alter this $J_{Dy\text{-}Cr}$ to the strongest value yield the best T_B values, offering design clues to improve the SMM characteristics in this family of complexes. Further, the substitution on the aromatic ring is found to be the more suitable approach to attain large U_{eff} and T_B compared to the alternation in the polyamine alcohol group for such class of complexes, where the variation on the terminal Dy^{III} coordination with more than eight coordination leads to the diminishing of SMM behaviour.

e) The most suitable combination of transition metal (TM) and Dy^{III}, along with suitable ligands, has been studied to optimise the SMM of butterfly complexes. Since the nature of TM-TM plays a dominating role, this can be further improved by enhancing this exchange e.g. by bringing into play the 4d and 5d TM ions which have more diffuse d orbitals. In our earlier report, we have incorporated the 4d–4f exchange in $\{Ru_2Dy_2\}$ butterfly complexes, however smaller U_{eff} and no T_B were observed above 2 K, this contradicting SMM behaviour was due to poor exchange between the Ru^{III}-Dy^{III} center, likely due to a single unpaired electron residing on the Ru^{III} center.[27] However, similar polynuclear 3d–4f complexes have been reported with stronger 3d–4f

View Article Online
DOI: 10.1039/D4QI01484G

ferromagnetic exchange containing Cu^{II} and Dy^{III} ions, [90, 91] adapting these geometries/ions could pave the way for higher T_B values. Furthermore, with such ferromagnetic exchange coupling between the 3d-4f metal centers, the 4f ions can also be varied to produce new series of SMMs involving lanthanide ions other than Dy^{III}.

Acknowledgements

We thank DST and SERB (SB/SJF/2019-20/12; CRG/2022/001697) for funding. AS thanks UGC/CSIR for the fellowship. M.S acknowledges the financial support from the Prime Ministers Research Fellowship(PMRF). KSM thanks the Australian Research Council for a Discovery grant.

References

1. Single-molecule magnets, G. Christou, D. Gatteschi, D. N. Hendrickson and R. Sessoli, *Mrs Bulletin*, 2000, **25**, 66-71.
2. High density data storage: Principle, Technology, and Materials, Y. Song and D. Zhu, *High density data storage: Principle, Technology, and Materials*, World Scientific, 2009.
3. Magnetic blocking temperature, D. York, *Earth Planet. Sci. Lett.*, 1978, **39**, 94-97.
4. Determination of the blocking temperature of magnetic nanoparticles: The good, the bad, and the ugly, I. J. Bruvera, P. Mendoza Zélis, M. Pilar Calatayud, G. F. Goya and F. H. Sánchez, *J. Appl. Phy.*, 2015, **118**, 184304.
5. Magnetic bistability in a metal-ion cluster, R. Sessoli, D. Gatteschi, A. Caneschi and M. Novak, *Nature*, 1993, **365**, 141-143.
6. Magnetic hysteresis up to 80 kelvin in a dysprosium metallocene single-molecule magnet, F.-S. Guo, B. M. Day, Y.-C. Chen, M.-L. Tong, A. Mansikkamäki and R. A. Layfield, *Science*, 2018, **362**, 1400-1403.
7. Mononuclear Dysprosium Alkoxide and Aryloxide Single-Molecule Magnets, V. S. Parmar, D. P. Mills and R. E. Winpenny, *Chem. Eur. J.*, 2021, **27**, 7625-7645.
8. Recent Developments in Lanthanide Single-Molecule Magnets, J. Lu, M. Guo and J. Tang, *Chem. Asian. J.*, 2017, **12**, 2772-2779.
9. Lanthanide single molecule magnets: progress and perspective, P. Zhang, L. Zhang and J. Tang, *Dalton. Trans.*, 2015, **44**, 3923-3929.
10. Lanthanide single-molecule magnets, D. N. Woodruff, R. E. Winpenny and R. A. Layfield, *Chem. Rev.*, 2013, **113**, 5110-5148.
11. Prediction of the quantised axis of rare-earth ions: the electrostatic model with displaced point charges, S.-D. Jiang and S.-X. Qin, *Inorg. Chem. Fron.*, 2015, **2**, 613-619.
12. Use of Advanced EPR Methods for the Study of Lanthanide and Actinide complexes, A.-M. Ariciu, *Use of Advanced EPR Methods for the Study of Lanthanide and Actinide complexes*, The University of Manchester (United Kingdom), 2019.
13. Molecular magnetic hysteresis at 60 kelvin in dysprosocenium, C. A. Goodwin, F. Ortu, D. Reta, N. F. Chilton and D. P. Mills, *Nature*, 2017, **548**, 439-442.
14. High-temperature magnetic blocking and magneto-structural correlations in a series of dysprosium (III) metallocenium single-molecule magnets, K. R. McClain, C. A. Gould, K. Chakarawet, S. J. Teat, T. J. Groshens, J. R. Long and B. G. Harvey, *Chem. Sci.*, 2018, **9**, 8492-8503.

View Article Online
DOI: 10.1039/D4QI01484G

15. A High-Performance Single-Molecule Magnet Utilising Dianionic Aminoborolide Ligands, J. C. Vanjak, B. O. Wilkins, V. Vieru, N. S. Bhuvanesh, J. H. Reibenspies, C. D. Martin, L. F. Chibotaru and M. Nippe, *J. Am. Chem. Soc.*, 2022, **144**, 17743-17747.
16. Quantum tunnelling of magnetisation and related phenomena in molecular materials, D. Gatteschi and R. Sessoli, *Angew, Chem. Int. Ed.*, 2003, **42**, 268-297.
17. Role of Magnetic Exchange Interactions in the Magnetization Relaxation of {3d–4f} Single-Molecule Magnets: A Theoretical Perspective, S. K. Singh, M. F. Beg and G. Rajaraman, *Chem. Eur. J.*, 2016, **22**, 672-680.
18. Strong exchange and magnetic blocking in N_2^{3-}-radical-bridged lanthanide complexes, J. D. Rinehart, M. Fang, W. J. Evans and J. R. Long, *Nat. Chem.*, 2011, **3**, 538-542.
19. Dinuclear Dysprosium(III) Single-Molecule Magnets with a Large Anisotropic Barrier, P. H. Lin, T. J. Burchell, R. Clérac and M. Murugesu, *Angew. Chem.*, 2008, **47**, 8848-8851.
20. Single-molecule magnet behaviour for an antiferromagnetically superexchange-coupled dinuclear dysprosium (III) complex, J. Long, F. Habib, P.-H. Lin, I. Korobkov, G. Enright, L. Ungur, W. Wernsdorfer, L. F. Chibotaru and M. Murugesu, *J. Am. Chem. Soc.*, 2011, **133**, 5319-5328.
21. A N_2^{3-} Radical-Bridged Terbium Complex Exhibiting Magnetic Hysteresis at 14 K, J. D. Rinehart, M. Fang, W. J. Evans and J. R. Long, *J. Am. Chem. Soc.*, 2011, **133**, 14236-14239.
22. Orbital interactions, electron delocalisation and spin coupling in iron-sulfur clusters, L. Noodleman, C. Peng, D. Case and J.-M. Mouesca, *Coord. Chem. Rev.*, 1995, **144**, 199-244.
23. The role of electronic delocalisation in transition metal complexes from the electron localisation function and the quantum theory of atoms in molecules viewpoints, E. Matito and M. Solà, *Coord. Chem. Rev.*, 2009, **253**, 647-665.
24. Magnetic exchange in {Gd III–radical} complexes: method assessment, mechanism of coupling and magneto-structural correlations, T. Gupta, T. Rajeshkumar and G. Rajaraman, *Phys. Chem. Chem. Phys.*, 2014, **16**, 14568-14577.
25. Are lanthanide-transition metal direct bonds a route to achieving new generation {3d–4f} SMMs?, A. Swain, A. Sen and G. Rajaraman, *Dalton. Trans.*, 2021, **50**, 16099-16109.
26. Ultrahard magnetism from mixed-valence dilanthanide complexes with metal-metal bonding, C. A. Gould, K. R. McClain, D. Reta, J. G. Kragskow, D. A. Marchiori, E. Lachman, E.-S. Choi, J. G. Analytis, R. D. Britt and N. F. Chilton, *Science*, 2022, **375**, 198-202.
27. Enhancing the barrier height for magnetisation reversal in 4d/4f $Ru^{III}_2Ln^{III}_2$ "butterfly" single molecule magnets (Ln = Gd, Dy) via targeted structural alterations, A. Swain, R. Martin, K. R. Vignesh, G. Rajaraman, K. S. Murray and S. K. Langley, *Dalton. Trans.*, 2021, **50**, 12265-12274.
28. Record high magnetic exchange and magnetisation blockade in Ln2@C79 N (Ln= Gd (III) and Dy (III)) molecules: a theoretical perspective, M. K. Singh, N. Yadav and G. Rajaraman, *Chem. Comm.*, 2015, **51**, 17732-17735.
29. Air-stable redox-active nanomagnets with lanthanide spins radical-bridged by a metal–metal bond, F. Liu, D. S. Krylov, L. Spree, S. M. Avdoshenko, N. A. Samoylova, M. Rosenkranz, A. Kostanyan, T. Greber, A. U. Wolter, B. Büchner, S. M. Avdoshenko and A. A. Popov *Nat. Comm.*, 2017, **8**, 16098.
30. Endohedral Metallofullerene as Molecular High Spin Qubit: Diverse Rabi Cycles in Gd2@C79N, Z. Hu, B.-W. Dong, Z. Liu, J.-J. Liu, J. Su, C. Yu, J. Xiong, D.-E. Shi, Y. Wang and B.-W. Wang, *J. Am. Chem. Soc.*, 2018, **140**, 1123-1130.
31. Effects of 3d–4f Magnetic Exchange Interactions on the Dynamics of the Magnetization of Dy^{III}-M^{II}-Dy^{III} Trinuclear Clusters, F. Pointillart, K. Bernot, R. Sessoli and D. Gatteschi, *Chem. Eur. J.*, 2007, **13**, 1602-1609.
32. 3d− 4f combined chemistry: synthetic strategies and magnetic properties, M. Andruh, J.-P. Costes, C. Diaz and S. Gao, *Inorg. Chem.*, 2009, **48**, 3342-3359.

View Article Online
DOI: 10.1039/D4QI01484G

33. Linear versus Bent 3d/4f-Heterometallic Clusters: The Carboxylate Effect on the Metal Topology and Magnetic Properties of Two $\{Mn^{III}_2Dy_2\}$ Complexes Supported by N-Naphthalidene-o-Aminophenol, K. N. Pantelis, K. H. Baka, J. Huang, C. P. Raptopoulou, V. Psycharis, K. R. Dunbar and T. C. Stamatatos, *Crys. Grow. & Des.*, 2023, **23**, 5301-5313.

34. Experimental and theoretical investigations of four 3d–4f butterfly single-molecule magnets, H.-H. Zou, L.-B. Sheng, F.-P. Liang, Z.-L. Chen and Y.-Q. Zhang, *Dalton. Trans.*, 2015, **44**, 18544-18552.

35. Tuning Quantum Tunneling in Isomorphic $\{M^{II}_2Dy^{III}_2\}$ "Butterfly" System via 3d-4f Magnetic Interaction, G.P. Li, H.-Z. Tang, R.-C. Gao, Y.-Y. Wang, X. Sun and K. Zhang, *Crys. Grow. & Des.*, 2023, **23**, 1575-1580.

36. Magnetic materials based on heterometallic $Cr^{II/III}$–Ln^{III} complexes, P. Shukla, S. Das, P. Bag and A. Dey, *Inorg. Chem. Front.*, 2023, **10**, 4322-4357.

37. A Family of $\{Cr^{III}_2Ln^{III}_2\}$ Butterfly Complexes: Effect of the Lanthanide Ion on the Single-Molecule Magnet Properties, S. K. Langley, D. P. Wielechowski, N. F. Chilton, B. Moubaraki and K. S. Murray, *Inorg. Chem.*, 2015, 54, 10497-10503.

38. Heterometallic Tetranuclear $[Ln^{III}_2Co^{III}_2]$ Complexes Including Suppression of Quantum Tunneling of Magnetization in the $[Dy^{III}_2Co^{III}_2]$ Single Molecule Magnet, S. K. Langley, N. F. Chilton, L. Ungur, B. Moubaraki, L. F. Chibotaru and K. S. Murray, *Inorg. Chem.*, 2012, **51**, 11873-11881.

39. A $\{Cr^{III}_2Dy^{III}_2\}$ single-molecule magnet: enhancing the blocking temperature through 3d magnetic exchange, S. K. Langley, D. P. Wielechowski, V. Vieru, N. F. Chilton, B. Moubaraki, B. F. Abrahams, L. F. Chibotaru and K. S. Murray, *Angew, Chem. Int. Ed.*, 2013, **52**, 12014-12019.

40. Single-Molecule Magnetism in a Family of $\{Co^{III}_2Dy^{III}_2\}$ Butterfly Complexes: Effects of Ligand Replacement on the Dynamics of Magnetic Relaxation, S. K. Langley, L. Ungur, N. F. Chilton, B. Moubaraki, L. F. Chibotaru and K. S. Murray, *Inorg. Chem.*, 2014, **53**, 4303-4315.

41. Modulation of slow magnetic relaxation by tuning magnetic exchange in $\{Cr_2Dy_2\}$ single molecule magnets, S. K. Langley, D. P. Wielechowski, V. Vieru, N. F. Chilton, B. Moubaraki, L. F. Chibotaru and K. S. Murray, *Chem. Sci.*, 2014, **5**, 3246-3256.

42. Heterometallic 3d–4f single-molecule magnets: ligand and metal ion influences on the magnetic relaxation, S. K. Langley, C. Le, L. Ungur, B. Moubaraki, B. F. Abrahams, L. F. Chibotaru and K. S. Murray, *Inorg. Chem.*, 2015, **54**, 3631-3642.

43. The first 4d/4f single-molecule magnet containing a $\{Ru^{III}_2Dy^{III}_2\}$ core, S. K. Langley, D. P. Wielechowski, V. Vieru, N. F. Chilton, B. Moubaraki, L. F. Chibotaru and K. S. Murray, *Chem. Comm.*, 2015, **51**, 2044-2047.

44. What do 3d-4f butterflies tell us? Y. Peng and A. K. Powell, *Coord. Chem. Rev.*, 2021, **426**, 213490.

45. Exploiting single-ion anisotropy in the design of f-element single-molecule magnets, J. D. Rinehart and J. R. Long, *Chem. Sci.*, 2011, **2**, 2078-2085.

46. On the importance of ferromagnetic exchange between transition metals in field-free SMMs: examples of ring-shaped hetero-trimetallic $[(LnNi_2)\{W(CN)_8\}]_2$ compounds, S. Dhers, J.-P. Costes, P. Guionneau, C. Paulsen, L. Vendier and J.-P. Sutter, *Chem. Comm.*, 2015, **51**, 7875-7878.

47. Exploring the Influence of Diamagnetic Ions on the Mechanism of Magnetization Relaxation in $\{Co^{III}_2Ln^{III}_2\}$ (Ln = Dy, Tb, Ho) "Butterfly" Complexes, K. R. Vignesh, S. K. Langley, K. S. Murray and G. Rajaraman, *Inorg. Chem.*, 2017, **56**, 2518-2532.

48. Structural design of easy-axis magnetic anisotropy and determination of anisotropic parameters of Ln(III)-Cu(II) single-molecule magnets, T. Kajiwara, M. Nakano, K. Takahashi, S. Takaishi and M. Yamashita, *Chem. Eur. J.*, 2011, 17, 196-205.

View Article Online
DOI: 10.1039/D4QI01484G

49. Density functional theory, M. Orio, D. A. Pantazis and F. Neese, *Photosynthesis research*, 2009, **102**, 443-453.
50. Density functional theory, E. Engel, Springer, 2011.
51. The CASSCF state interaction method, P. A. Malmqvist and B. O. Roos, *Chem. Phy. Lett.*, 1989, **155**, 189-194.
52. Ab initio calculation of anisotropic magnetic properties of complexes. I. Unique definition of pseudospin Hamiltonians and their derivation, L. F. Chibotaru and L. Ungur, *J. Chem. Phys.*, 2012, **137**, 064112.
53. Rigaku Oxford Diffraction, CrysAlis, *Yarnton, England*, 2009.
54. SHELXL-97, G. Sheldrick, *J. Appl. Crys.*, 1997.
55. Blu-Ice and the Distributed Control System: software for data acquisition and instrument control at macromolecular crystallography beamlines, T. M. McPhillips, S. E. McPhillips, H.-J. Chiu, A. E. Cohen, A. M. Deacon, P. J. Ellis, E. Garman, A. Gonzalez, N. K. Sauter and R. P. Phizackerley, *Journal of synchrotron radiation*, 2002, **9**, 401-406.
56. Automatic processing of rotation diffraction data from crystals of initially unknown symmetry and cell constants, W. Kabsch, *J. Appl. Crys.*, 1993, **26**, 795-800.
57. SHELXL-97, G. Sheldrick, *Program for crystal structure refinement*, 1997.
58. MOLCAS 8: New capabilities for multiconfigurational quantum chemical calculations across the periodic table, F. Aquilante, J. Autschbach, R. K. Carlson, L. F. Chibotaru, M. G. Delcey, L. De Vico, I. Fdez. Galván, N. Ferré, L. M. Frutos and L. Gagliardi, *J. Comp. Chem.*, 2016, **37**, 506-541.
59. The restricted active space (RAS) state interaction approach with spin–orbit coupling, P. A. Malmqvist, B. O. Roos and B. Schimmelpfennig, *Chem. Phys. Lett.*, 2002, **357**, 230-240.
60. How to link theory and experiment for single-chain magnets beyond the Ising model: magnetic properties modelled from ab initio calculations of molecular fragments, M. Böhme and W. Plass, *Chem. Sci.*, 2019, **10**, 9189-9202.
61. Ab initio crystal field for lanthanides, L. Ungur and L. F. Chibotaru, *Chem. Eur. J.*, 2017, **23**, 3708-3718.
62. Gaussian 16, Revision A.02, M. J. Frisch, G. W. Trucks, H. B. Schlegel, G. E. Scuseria, M. A. Robb, J. R. Cheeseman, G. Scalmani, V. Barone, G. A. Petersson, H. Nakatsuji, X. Li, M. Caricato, A. Marenich, J. Bloino, B. G. Janesko, R. Gomperts, B. Mennucci, H. P. Hratchian, J. V. Ortiz, A. F. Izmaylov, J. L. Sonnenberg, D. Williams-Young, F. Ding, F. Lipparini, F. Egidi, J. Goings, B. Peng, A. Petrone, T. Henderson, D. Ranasinghe, V. G. Zakrzewski, J. Gao, N. Rega, G. Zheng, W. Liang, M. Hada, M. Ehara, K. Toyota, R. Fukuda, J. Hasegawa, M. Ishida, T. Nakajima, Y. Honda, O. Kitao, H. Nakai, T. Vreven, K. Throssell, J. A. Montgomery, Jr., J. E. Peralta, F. Ogliaro, M. Bearpark, J. J. Heyd, E. Brothers, K. N. Kudin, V. N. Staroverov, T. Keith, R. Kobayashi, J. Normand, K. Raghavachari, A. Rendell, J. C. Burant, S. S. Iyengar, J. Tomasi, M. Cossi, J. M. Millam, M. Klene, C. Adamo, R. Cammi, J. W. Ochterski, R. L. Martin, K. Morokuma, O. Farkas, J. B. Foresman, and D. J. Fox, *Inc., Wallingford CT*, 2009, **121**, 150-166.
63. Broken symmetry analysis of spin coupling in iron-sulfur clusters, L. Noodleman, D. A. Case and A. Aizman, *J. Am. Chem. Soc.*, 1988, **110**, 1001-1005.
64. Density-functional exchange-energy approximation with correct asymptotic behaviour, A. D. Becke, *Phys. Rev. A*, 1988, **38**, 3098.
65. Density functional theory of electronic structure, W. Kohn, A. D. Becke and R. G. Parr, *J. Phy. Chem.*, 1996, **100**, 12974-12980.
66. Azide-Coordination in Homometallic Dinuclear Lanthanide(III) Complexes Containing Nonequivalent Lanthanide Metal Ions: Zero-Field SMM Behavior in the Dysprosium Analogue, P. Kumar, S. Biswas, A. Swain, J. Acharya, V. Kumar, P. Kalita, J. F. Gonzalez, O. Cador, F. Pointillart and G. Rajaraman, *Inorg. Chem.*, 2021, **60**, 8530-8545.

View Article Online
DOI: 10.1039/D4QI01484G

67. Theoretical study of the magnetic interaction for M–O–M type metal oxides. Comparison of broken-symmetry approaches, T. Onishi, Y. Takano, Y. Kitagawa, T. Kawakami, Y. Yoshioka and K. Yamaguchi, *Polyhedron*, 2001, **20**, 1177-1184.
68. Ab initio computations of effective exchange integrals for H–H, H–He–H and Mn2O2 complex: comparison of broken-symmetry approaches, T. Soda, Y. Kitagawa, T. Onishi, Y. Takano, Y. Shigeta, H. Nagao, Y. Yoshioka and K. Yamaguchi, *Chem. Phy. Lett.*, 2000, **319**, 223-230.
69. The origin of nonmagnetic Kramers doublets in the ground state of dysprosium triangles: evidence for a toroidal magnetic moment, L. F. Chibotaru, L. Ungur and A. Soncini, *Angew. Chem.*, 2008, **120**, 4194-4197.
70. Structure, Magnetism, and Theoretical Study of a Mixed-Valence CoII3CoIII4 Heptanuclear Wheel: Lack of SMM Behavior despite Negative Magnetic Anisotropy, L. F. Chibotaru, L. Ungur, C. Aronica, H. Elmoll, G. Pilet and D. Luneau, *J. Am. Chem. Soc.*, 2008, **130**, 12445-12455.
71. Reduced scaling in electronic structure calculations using Cholesky decompositions, H. Koch, A. Sánchez de Merás and T. B. Pedersen, *J. Chem. Phys.*, 2003, **118**, 9481-9484.
72. Douglas–Kroll–Hess Theory: a relativistic electrons-only theory for chemistry, M. Reiher, *Theor. Chem. Acc.*, 2006, **116**, 241-252.
73. Role of Ab Initio calculations in the design and development of lanthanide based single molecule magnets, T. Gupta, M. K. Singh and G. Rajaraman, *Organometallic Magnets*, 2019, 281-354.
74. New relativistic ANO basis sets for transition metal atoms, B. O. Roos, R. Lindh, P.-Å. Malmqvist, V. Veryazov and P.-O. Widmark, *J. Phys. Chem. A*, 2005, **109**, 6575-6579.
75. The ANO-R basis set, J. P. Zobel, P.-O. Widmark and V. Veryazov, *J. Chem. Theo. Comp.*, 2019, **16**, 278-294.
76. All-electron scalar relativistic basis sets for the lanthanides, D. A. Pantazis and F. Neese, *J. Chem. Theo. Comp.*, 2009, **5**, 2229-2238.
77. Effective core potential methods for the lanthanides, T. R. Cundari and W. J. Stevens, *J. Chem. Phys.*, 1993, **98**, 5555-5565.
78. Basis set exchange: a community database for computational sciences, K. L. Schuchardt, B. T. Didier, T. Elsethagen, L. Sun, V. Gurumoorthi, J. Chase, J. Li and T. L. Windus, *J. Chem. Info. Model.*, 2007, **47**, 1045-1052.
79. Fully optimised contracted Gaussian basis sets of triple zeta valence quality for atoms Li to Kr, A. Schäfer, C. Huber and R. Ahlrichs, *J. Chem. Phys.*, 1994, **100**, 5829-5835.
80. The ORCA program system, F. Neese, *WIRES Comp. Mol. Sci*, 2012, **2**, 73-78.
81. Continuous shape measures as a stereochemical tool in organometallic chemistry, J. Cirera, E. Ruiz and S. Alvarez, *Organometallics*, 2005, **24**, 1556-1562.
82. Local properties of quantum chemical systems: The LoProp approach, L. Gagliardi, R. Lindh and G. Karlström, *J. Chem. Phys.*, 2004, **121**, 4494-4500.
83. Transformation relations for the conventional Okq and normalised O'kq Stevens operator equivalents with k= 1 to 6 and-k⩽ q⩽ k, C. Rudowicz, *J. Phy. Chem. C.*, 1985, **18**, 1415.
84. Fluoride-Bridged {GdIII3MIII2} (M=Cr, Fe, Ga) Molecular Magnetic Refrigerants, K. S. Pedersen, G. Lorusso, J. J. Morales, T. Weyhermüller, S. Piligkos, S. K. Singh, D. Larsen, M. Schau-Magnussen, G. Rajaraman and M. Evangelisti, *Angew, Chem. Int. Ed.*, 2014, **53**, 2394-2397.
85. Angular dependence of the exchange interaction in fluoride-bridged Gd III–Cr III complexes, S. K. Singh, K. S. Pedersen, M. Sigrist, C. A. Thuesen, M. Schau-Magnussen, H. Mutka, S. Piligkos, H. Weihe, G. Rajaraman and J. Bendix, *Chem. Comm.*, 2013, **49**, 5583-5585.
86. Theoretical studies on {3d-Gd} and {3d-Gd-3d} complexes: Effect of metal substitution on the effective exchange interaction, S. K. Singh, T. Rajeshkumar, V. Chandrasekhar and G. Rajaraman, *Polyhedron*, 2013, **66**, 81-86.

View Article Online
DOI: 10.1039/D4QI01484G

87. A computational perspective on magnetic coupling, magneto-structural correlations and magneto-caloric effect of a ferromagnetically coupled {GdIII–GdIII} Pair, T. Rajeshkumar, S. K. Singh and G. Rajaraman, *Polyhedron*, 2013, **52**, 1299-1305.
88. SMM Behaviour of the Butterfly $\{Cr^{III}_2Dy^{III}_2\}$ Pivalate Complex and Magneto-structurally Correlated Relaxation Thermal Barrier, J. H. Mecchia Ortiz, D. Cabrosi, L. M. Carrella, E. Rentschler and P. Alborés, *Chem. Eur. J.*, 2022, **28**, e202201450.
89. Interplay of strongly anisotropic metal ions in magnetic blocking of complexes, L. Ungur, M. Thewissen, J.-P. Costes, W. Wernsdorfer and L. F. Chibotaru, *Inorg. Chem.*, 2013, **52**, 6328-6337.
90. Two Octanuclear $\{Cu_4Ln_4\}$ (Ln = Dy or Tb) Complexes with a Butterfly-Shaped Unit Exhibiting Zero-Field Single-Molecule Magnet Behavior, X. Zhao, G. Li, J. Ma and W. Liu, *Inorg. Chem.*, 2020, **59**, 2328-2336.
91. Oximate-bridged trinuclear Dy− Cu− Dy complex behaving as a single-molecule magnet and its mechanistic investigation, F. Mori, T. Nyui, T. Ishida, T. Nogami, K.-Y. Choi and H. Nojiri, *J. Am. Chem. Soc.*, 2006, **128**, 1440-1441.

Data availability statement

View Article Online
DOI: 10.1039/D4QI01484G

The data supporting this article have been included as part of the Supplementary Information.

Crystallographic details are available in the Supporting Information (SI) in CIF format. CCDC numbers 866839, 994294–994297, 1495741–1495743 and 2268871-2268878. These data can be obtained free of charge from the Cambridge Crystallographic Data Centre via www.ccdc.cam.ac.uk/data_request/cif.